NASA CR-137719

SOLUTIONS TO KÜSSNER'S INTEGRAL EQUATION IN UNSTEADY FLOW USING LOCAL BASIS FUNCTIONS

J. A. Fromme and D. W. Halstead

September 1975

Final Report (Task IV, Item 2)

Prepared under contract NAS2-7729 by

Boeing Commercial Airplane Company
P.O. Box 3707
Seattle, Washington 98124

for
Ames Research Center
NATIONAL AERONAUTICS AND SPACE ADMINISTRATION

11 INCH CROPS

1. Report No.	2. Government Accession No.	3. Recipient's Catalog No.
CR-137719		

4. Title and Subtitle

SOLUTIONS TO KÜSSNER'S INTEGRAL EQUATION IN UNSTEADY FLOW USING LOCAL BASIS FUNCTIONS

5. Report Date: September 1975

6. Performing Organization Code:

7. Author(s)

J. A. Fromme and D. W. Halstead

8. Performing Organization Report No.: D6-43599

9. Performing Organization Name and Address

Boeing Commercial Airplane Company
Seattle, Washington 98124

10. Work Unit No.:

11. Contract or Grant No.: NAS2-7729

12. Sponsoring Agency Name and Address

National Aeronautics and Space Administration
Washington, D.C. 20546

13. Type of Report and Period Covered: Final Report Task IV, Item 2

14. Sponsoring Agency Code:

15. Supplementary Notes

16. Abstract

The computational procedure and numerical results are presented for a new method to solve Küssner's integral equation in the case of subsonic compressible flow about harmonically oscillating planar surfaces with controls. Küssner's equation is a linear transformation from pressure to normalwash. The unknown pressure is expanded in terms of prescribed basis functions and the unknown basis function coefficients are determined in the usual manner by satisfying the given normalwash distribution either collocationally or in the complex least squares sense. The present method of solution differs from previous ones in that the basis functions are defined in a continuous fashion over a relatively small portion of the aerodynamic surface and are zero elsewhere. This method, termed the local basis function method, combines the smoothness and accuracy of distribution methods with the simplicity and versatility of panel methods. Predictions by the local basis function method for unsteady flow are shown to be in excellent agreement with other methods. Also, potential improvements to the present method and extensions to more general classes of solutions are discussed.

17. Key Words (Suggested by Author(s))	18. Distribution Statement
Aerodynamics, Subsonic, Compressible, Unsteady, Flutter	Unclassified-Limited

19. Security Classif. (of this report)	20. Security Classif. (of this page)	21. No. of Pages	22. Price*
Unclassified	Unclassified	68	

*For sale by the National Technical Information Service, Springfield, Virginia 22151

CONTENTS

FIGURES

TABLES

SOLUTIONS TO KÜSSNER'S INTEGRAL EQUATION IN UNSTEADY FLOW USING LOCAL BASIS FUNCTIONS

J. A. Fromme and D. W. Halstead
Boeing Commercial Airplane Company

1.0 SUMMARY

The computational procedure and numerical results are presented for a new method to solve Küssner's integral equation in the case of subsonic compressible flow about harmonically oscillating planar surfaces with controls. Since Küssner's equation is a linear transformation from pressure to normalwash, the unknown pressure is expanded in terms of prescribed basis functions; the unknown basis function coefficients are determined in the usual manner by satisfying the given normalwash distribution, either collocationally or in the complex least squares sense. The present method of solution differs from previous ones in that the basis functions are defined in a continuous fashion over a relatively small portion of the aerodynamic surface and are zero elsewhere. This method, termed the local basis function method, combines the smoothness and accuracy of distribution methods with the simplicity and versatility of panel methods. Predictions by the local basis function method for unsteady flow are shown herein to be in excellent agreement with other methods. Also, potential improvements to the present method and extensions to more general classes of solutions are discussed.

2.0 INTRODUCTION

Aeroelastic analysis of flight structures involves the coupled dynamic response of structural and aerodynamical media. Within the confines of linear aeroelasticity, the coupling is determined by the matrix of energy that is transmitted across the body-fluid interface in the form of mechanical work done as the body deforms in one mode against the pressure due to another mode. This matrix, called the generalized aerodynamic force coefficient matrix, depends for its calculation upon knowledge of the unsteady pressure distribution.

The pressure distribution may be calculated by various methods. For a comprehensive discussion of these methods, the interested reader is referred to articles by Ashley and Rodden (ref. 1); Landahl and Stark (ref. 2); Ashley, Widnall, and Landahl (ref. 3); and to the more recent work of Morino (ref. 4). The particular method of the present study is a combination of two previous methods: (1) the classical pressure-normalwash method originating with Küssner (ref. 5) and developed further by Watkins, Runyan, Woolston, Cunningham, Hsu, Rowe, and others (refs. 6, 7, 8, 9, and 10); and (2) the splined local basis functions recently developed by Mercer, Weber, and others (refs. 11 and 12) for the case of steady flow. This formulation using local basis functions to solve the unsteady Küssner integral equation combines the smoothness and accuracy of distribution methods with the simplicity and versatility of panel methods. The present study is

applied to the solution of subsonic, compressible flow problems about oscillating planar surfaces with controls, although the mathematical methods employed apply to a larger class of solutions such as multiple nonplanar surfaces, etc.

Let S denote an aerodynamical lifting surface contained in, say, the xy-plane and immersed in an ideal fluid of density ρ and sonic speed a. A rectangular cartesian coordinate system (oxyz) is fixed with respect to the referential surface configuration. S is assumed to translate with respect to the fluid at uniform subsonic velocity V in the negative x-direction and to perform simple harmonic oscillations in the direction normal to S and at a circular frequency of ω radians per second. Then, under the usual assumptions, the method of acceleration potential (ref. 13) may be used in conjunction with Green's identities to obtain the well-known Küssner integral equation, which states that the normal components of velocity of the fluid and of the body are equal at the surface. Mathematically, Küssner's equation

$$w(x,y) = -\frac{1}{4\pi\rho V} \iint_{(\xi,\eta)\in S} K(x-\xi, y-\eta)\, p(\xi,\eta)\, dA \qquad (1)$$

is a linear transformation from pressure p to normalwash w, where the indicated surface integration is in the sense of Hadamard (ref. 14). The kernel of the transformation (ref. 6) is given by

$$K(x,y) = \frac{1}{y^2} \exp\left(-\frac{i\omega x}{V}\right)\left\{-\frac{\omega|y|}{V}\left[K_1\left(\frac{\omega|y|}{V}\right) + \frac{i\pi}{2} I_1\left(\frac{\omega|y|}{V}\right) - \frac{i\pi}{2} L_1\left(\frac{\omega|y|}{V}\right) - i\right]\right.$$

$$\left. - i\int_0^{\frac{x-M\,r_\beta}{\beta^2|y|}} \exp\left(\frac{i\omega|y|\tau}{V}\right)\frac{\tau d\tau}{\sqrt{1+\tau^2}} - \frac{x}{r_\beta}\exp\left[\frac{i\omega(x-M\,r_\beta)}{\beta^2 V}\right]\right\} \qquad (2)$$

where M is Mach number, $r_\beta = \sqrt{x^2+\beta^2y^2}$, and where I_1 and K_1 are the modified Bessel functions of the first order and L_1 is the Struve function (ref. 15).

The solution to equation (1) proceeds by expanding the unknown pressure in terms of a prescribed set $\{p_n\}$ of basis functions

$$p(\xi,\eta) = \tfrac{1}{2}\rho V^2 \sum b_n p_n(\xi,\eta) \qquad (3)$$

and determining the unknown $\{b_n\}$ by satisfying equation (1), either collocationally or in the complex least squares sense, on a set $\{(x_m,y_m)\}$ of normalwash control points:

$$\underset{N_w \times 1}{\left\{\frac{w(x_m,y_m)}{V}\right\}} = -\frac{1}{8\pi}\underset{N_w \times N_p,\ N_w \geq N_p}{\left[\iint_{(\xi,\eta)\in S} K(x_m-\xi, y_m-\eta)\, p_n(\xi,\eta)\, dA\right]} \underset{N_p \times 1}{\{b_n\}}, \qquad (4)$$

where N_w and N_p denote the number of normalwash points and pressure basis functions, respectively.

3.0 SYMBOLS

Symbols used are listed below. To the right of the symbols are listed their definitions, or the section, equation, or reference in which they are defined or first appear.

Care has been taken to not use the same symbol for different meanings. There are a few exceptions, but it should be clear from the context what is meant.

Any *dimensionally consistent choice of units is permissible—dimensional or* nondimensional.

$A, \tilde{A}$	areas of primary and secondary surfaces, respectively, section A.6
$AIC^{\zeta}_{\ell m}, AIC^{\xi}_{\ell m}, AIC^{\eta}_{\ell m}$	aerodynamic influence coefficient matrices of chordwise pitching moment, spanwise rolling moment, and vertical lifting force, respectively, on panel ℓ due to normalwash at point m, equations (A-23) through (A-25)
A_{rs}	generalized aerodynamic force coefficient matrix, equation (A-26)
AR	aspect ratio
$[a,b], [a_*, b_*]$	spanwise intervals of integration, equations (7) and (34)
b_n	pressure basis function coefficients, equation (3)
C_L, C_{L_H}	lift coefficient for primary and secondary surfaces, respectively, equations (A-12) and (A-13)
$C_{L_\alpha}, C_{L_\delta}$	derivatives of lift coefficient with respect to angle of attack and angle of control deflection, respectively
c, c_F	chord length, flap chord length, figure 27
$c(\eta)$	panel chord length as a function of spanwise coordinate, equations (32) and (33)
$[C_{mn}]$	coefficient matrix relating normalwash at point m due to nth pressure basis function, equation (A-18)
$c_\ell(\eta), c_{\ell_H}(\eta)$	spanwise sectional lift distribution for primary and secondary surfaces, respectively, equations (A-8) and (A-9)
ℓ^{ζ}	vertical force on panel ℓ with dynamic pressure factored out, equation (A-20)

$G(x,y,\eta)$	streamwise integral, used for calculating finite part of infinite integral, equation (7)
$G_{,\eta}(x,y,\eta)$	derivative of G with respect to its third coordinate
$G_*(x,y\eta)$	doubly differenced, Cauchy-integrable form of $G(x,y,\eta)$, equation (8)
$\hat{G}_*(x,y,\eta)$	$G_*(x,y,\eta)$ with logarithmic singularity removed, figure 9
I_1	modified Bessel function of the first kind and first order, equation (2)
K_1	modified Bessel function of the second kind and first order, equation (2)
k	reduced frequency, $\omega\ell/V$
L_1	Struve function of the first order, equation (2)
ℓ	characteristic length; also panel index, section A.6.7
M	Mach number
M_ℓ^ξ, M_ℓ^η	pitching and rolling moments acting on panel ℓ, section A.6.7
m	normalwash index, equation (4)
$N(\bar{n})$	the set of indices of basis functions whose supports nontrivially intersect the panel with index n, equation (A-6)
$\bar{N}(n)$	the set of indices of panels contained in the support of the nth basis function, equation (A-5)
N_p, N_w	number of basis functions and number of normalwash points, respectively, equation (4)
N_L	number of loading panels, section A.6.7
N_c, N_s	the numbers of rows and columns, respectively, of panels covering the surface
n	basis function index, equation (3)
p_n	pressure basis function, equation (3)
P_ℓ	loading panel ℓ, section A.6.7

$R, \tilde{R}$	primary and secondary surface planforms, respectively, figure A-8
R_n	support of the nth pressure basis function, equation (A-2)
R_n^*	reflection of R_n, figure A-2
S	aerodynamic surface
V	freestream velocity, equation (1)
$[W]$	diagonal matrix of least squares weighting factors, equation (A-2)
w	fluid velocity normal to aerodynamic surface
X_n	characteristics function for support of the nth basis function, with a symmetry condition, equation (A-4)

X_μ	streamwise basis function, equation (6)
(x,y,z)	streamwise, spanwise, and vertical coordinates
(x_L, y_L)	leading-edge coordinates, figure A-6
(x_m, y_m)	normalwash points, equation (4)
$\bar{X}_{cp}$	streamwise center of pressure, referred to local chord
y_0, y_1, y_2	spanwise coordinates in fairing, figure A-7
Y_ν	spanwise basis function, equation (6)

Greek Symbols

α	angle of attack, radians
β	$\sqrt{1 - M^2}$, equation (2)
ΔC_P	pressure difference coefficient, figure 22
δ	flap deflection in radians, section 3.4
δ_F	fairing width ratio, figure A-7
ζ	vertical spatial coordinate, section A.6.7

η	horizontal spatial coordinate, section A.6.7
$\eta_{cp}, \tilde{\eta}_{cp}$	spanwise center of pressure for primary and secondary surface, respectively, equations (A-16) and (A-17)
η_L, η_R	left and right planform extremities, figure A-8
$\tilde{\eta}_L, \tilde{\eta}_R$	left and right control surface edges, figure A-8
θ	streamwise Multhopp angle, equation (35)
Λ	sweepback angle, section 3.5
μ	row index of the panel cover, equation (5)
$\mu(x,y)$	Mesa function, equation (27)
ν	column index of the panel cover, equation (5)
ξ	streamwise coordinate, equation (1)
$\bar{\xi}$	local panel coordinate, zero at forward edge, unity at aft edge, equation (21)
$\vec{\xi}$	three-dimensional spatial coordinate, equation (10)
$\xi_{cp}, \tilde{\xi}_{cp}$	streamwise center of pressure for primary and secondary surfaces, respectively, equations (A-14) and (A-15)
$\xi_F(\eta), \xi_A(\eta), \xi_M(\eta)$	forward, aft, and midedges, respectively, of a surface
$\tilde{\xi}_F, \tilde{\xi}_A$	forward and aft edges, respectively, of the secondary surface, figure A-8
ρ	density
τ	dummy variable of integration, equation (1)
$\phi(x,y)$	indefinite integral of the mesa function, equation (28)
ψ	indefinite moment of the mesa function, equation (29)
ω	frequency of structural oscillation, radians per second, equation (8)
$\omega_{\mu\nu}$	aerodynamic panel, figure 1

4.0 DESCRIPTION OF PRESENT METHOD

4.1 LOCAL BASIS FUNCTION METHOD

A major difficulty with the kernel function methods has been in the selection of efficient and general pressure basis functions. Early solutions were as suggested by Küssner, in which the basis functions were products, $p_n = X_n Y_n$ of chordwise functions X_n selected according to two-dimensional theory and spanwise functions Y_n selected according to lifting line theory. However, as analysis planforms became more realistic, especially with the incorporation of controls, the need for a more rational approach to the selection of basis functions became increasingly apparent. A major improvement was provided by Landahl (ref. 16), using the method of asymptotic expansions to exhibit the precise form of singularities in pressure that must be present along planform and control boundaries for the necessary jump discontinuities in boundary conditions there to be satisfied. An extension to Landahl's mathematical analysis in the case of swept hinge lines has been pointed out very recently by Rowe (ref. 10) and has resulted in improved accuracy and improved agreement with experiment.

The pressure basis functions of Küssner (ref. 5); Watkins, Runyan, Woolston, and Cunningham (refs. 6 and 7); Hsu (ref. 8); Rowe (refs. 9 and 10); and others may be termed global in the sense that the basis functions are defined over the entire planform. An inherent difficulty with the use of global basis functions is that the presence of local planform features such as controls, etc., affect the formulation of each basis function everywhere on the planform. An improvement may be offered by the use of local basis functions, which are defined over relatively small subsets of the planform and are zero elsewhere.

Consider the surface S shown in figure 1. S is represented by a set of panels $\{\omega_{\mu\nu}\}$ arranged into N_C rows and N_S columns. It is convenient to index the panels by double subscripts as well as single subscripts.

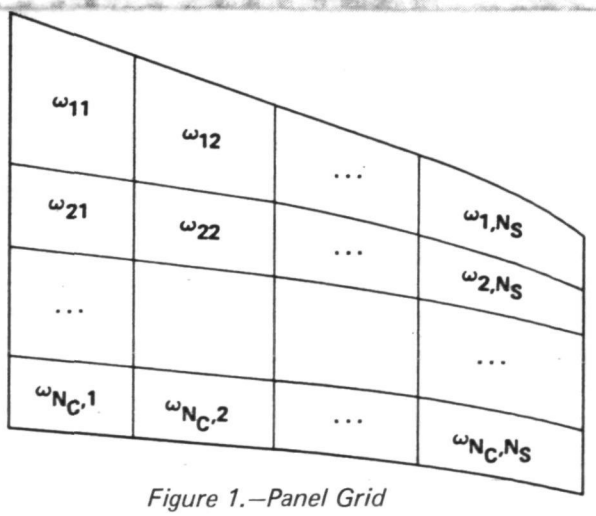

Figure 1.—Panel Grid

The transformation from single to double subscripts is given by:

$$n = \nu + (\mu - 1)N_S; \quad 1 \leq \mu \leq N_C, \quad 1 \leq \mu \leq N_S \qquad (5)$$

It is convenient to use the same subscript equivalence for defining local basis functions as separable products,

$$P_n(\xi,\eta) = X_\mu(\bar{x})Y_\nu(\eta); \quad 1 \leq \mu \leq N_C, \quad 1 \leq \nu \leq N_S \qquad (6)$$

where $\bar{x}(\xi,\eta)$ is a local chordwise coordinate, where each X_μ is a continuous, piecewise linear spline in the local chordwise coordinate, and where each Y_ν is a continuously differentiable, piecewise quadratic spline in the spanwise coordinate. Since the basis functions and panels have the same index set, the number of basis functions equals the number of panels and, therefore, the number of normalwash control points must equal or exceed the number of panels.

4.1.1 CHORDWISE FUNCTIONS

For a given value of y, the support* of X_μ is (1) row 1 of panels if $\mu = 1$, and (2) rows $\mu-1$ and μ of panels if $\mu = 1$. The chordwise functions are depicted in figure 2. X_1 is defined over the first row of panels and has unit value at the panel leading edge and zero value at the panel trailing edge. For $\mu > 1$ each X_μ is defined over two panel rows, has zero value at both the leading edge of the front panel and the trailing edge of the aft panel, and has unit value at the intersection of the front and rear panels.

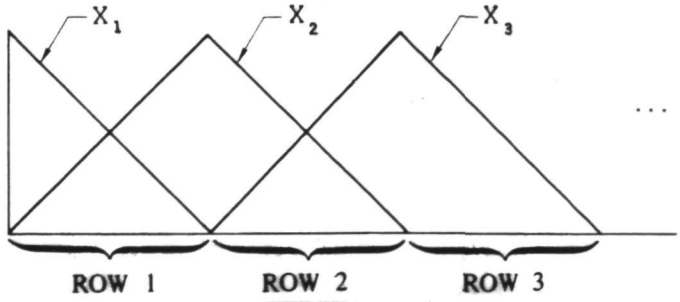

Figure 2.—Chordwise Functions

*The support of a function is the closure of the set on which the function is nonzero.

4.1.2 SPANWISE FUNCTIONS

The support of Y_ν is columns 1 and 2 of panels if $\nu = 1$; columns $\nu - 1, \nu$, and $\nu + 1$ if $1 < \nu < N_S$; and columns $N_S - 1$ and N_S if $\nu = N_S$. The spanwise functions are depicted in figure 3.

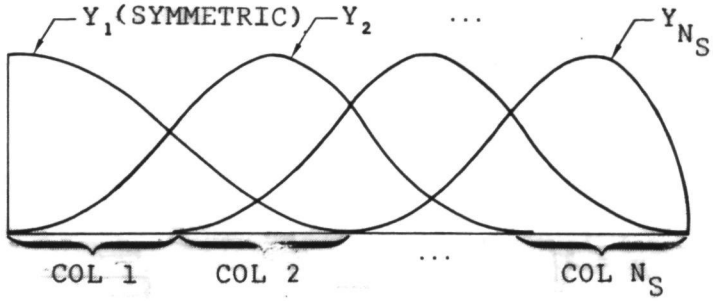

Figure 3.—Spanwise Functions

Each Y_ν has unit amplitude and is continuously differentiable across panel boundaries. If $1 < \nu < N_S$, Y_ν has zero value and at the left and right extremities of its support. If $\nu = N_S$, Y_ν has zero value and slope on the left and zero value on the right. If $\nu = 1$, Y_ν has zero value and slope on the right and zero slope on the left if that edge is symmetrically reflective, but zero value instead if that edge is antisymmetrically reflective or free. (This case is not illustrated in figure 3.)

4.1.3 OBSERVATIONS ON LOCAL BASIS FUNCTIONS

The above completely defines the pressure basis functions used in the present study. A typical pressure basis function is shown in figure 4. Several observations may be noted in regard to this set of functions.

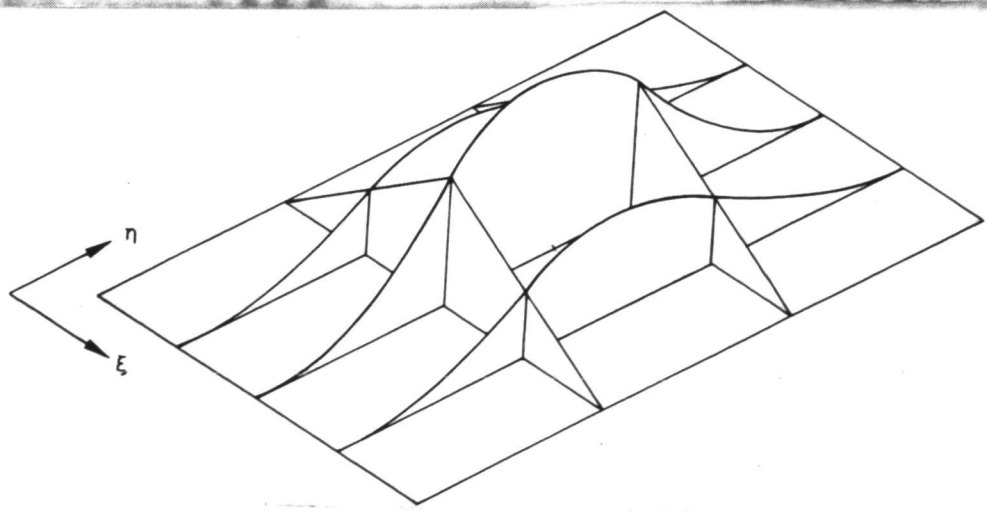

Figure 4.—Local Basis Function

1. It is a basis because it is linearly independent.
2. It is complete in the limit as the maximum panel dimension approaches zero.
3. It may be extended topologically to nonplanar surfaces.
4. Finite sums, used in practice, provide polygonal approximations chordwise and quadratic approximations spanwise.
5. Further additions such as incorporation of shape factors based on the Landahl-Rowe singularities can be made in a straightforward manner.

4.2 INTEGRATION OF DIPOLE SINGULARITY

The coefficient matrix of equation (4) is evaluated using Gaussian quadrature as in reference 17. In this operation the kernel function, equation (2), is separated into nonsingular and singular terms—equation (9) of reference 17. There are three singular terms identified as dipole, square root, and logarithmic singularity terms. The nonsingular terms as well as the square root and logarithmic singularity terms are readily evaluated. The dipole singularity term, however, requires special attention.

The dipole singularity term is expanded as

$$-\fint_a^b \frac{G(x,y,\eta)}{(y-\eta)^2}\,d\eta = \int_a^b G_*(x,y,\eta)\,d\eta + G(x,y,y)\left(\frac{1}{y-a}+\frac{1}{b-y}\right) + G_{,\eta}(x,y,y)\log\left|\frac{y-a}{b-y}\right|, \tag{7}$$

where the subscript $,\eta$ denotes partial differentiation, where G is the chordwise integral of the dipole singularity times the pressure, and where

$$G_*(x,y,\eta) = \frac{1}{y-\eta}\left[\frac{G(x,y,y)-G(x,y,\eta)}{y-\eta} - G_{,\eta}(x,y,y)\right] \tag{8}$$

The method for evaluating (ref. 8), described in section 5.1, has produced numerical results in the present computer code that have a maximum error of less than 0.10%.

The coefficient matrix in equation (4) is defined in terms of the pressure basis function index and the normalwash control point index. However, when local basis functions are employed, it is preferable to index the calculations by panels rather than by basis functions to avoid unnecessary repetitions in calculating the values of the kernel function. It is consequently necessary to determine exactly which basis functions are supported by each given panel. The required transformations between indices may be obtained in a straightforward fashion from equation (5). Also, it has been found that all coefficient matrix inversions using local basis functions have been well conditioned.

5.0 COMPUTER RESULTS

Computer results are presented for six problems: (1) a very simple steady-state problem in which the intermediate mathematical accuracy is evaluated; (2) a less simple steady-state problem, also in which the intermediate mathematical accuracy is evaluated; (3) a nonsteady problem in which convergence is studied and the results are compared with another code; (4) a nonsteady control surface problem in which the results are compared with another code; (5) a series of asymmetric planforms consisting of skewed parallelograms; and (6) the frequency response of a large, subsonic jet transport to gust loading. Problems (1) and (2) are basic checkout problems in which the numerical results were checked by separate calculations, whereas problems (3) to (6) are problems designed to validate the program by comparison with the results of other methods. The computer code used for the present study is a numerical research code referred to as RRX.

5.1 CHECKOUT PROBLEM ONE

The purpose of the first checkout problem, CP1, is to provide an accurate, closed-form comparison for the simplest possible problem. The planform and problem description are defined by figure 5.

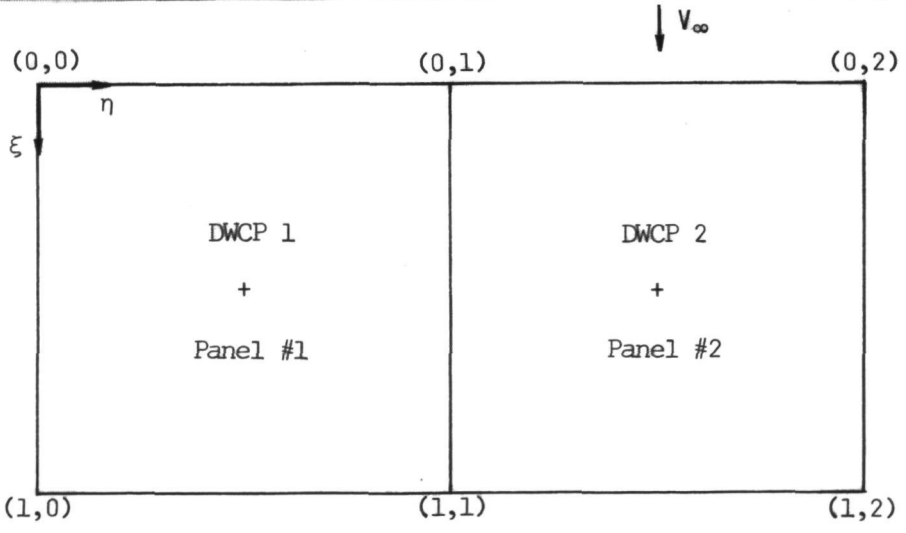


```
Simplest Possible Case
  k = 0  2 panels, run as an asymmetrical problem
  M = 0
mid panel downwash points
uniform angle of attack
```

Figure 5.—Planform for Checkout Problem One

For this problem, the coefficient matrix in

$$-\frac{1}{8\pi}\begin{bmatrix} C_{11} & C_{12} \\ C_{21} & C_{22} \end{bmatrix}\begin{Bmatrix} b_1 \\ b_2 \end{Bmatrix} = \begin{Bmatrix} \alpha_1 \\ \alpha_2 \end{Bmatrix} \tag{9}$$

is doubly symmetric, i.e.,

$$C_{11} = C_{22} \quad \& \quad C_{12} = C_{21} \tag{10}$$

and for uniform downwash ($\alpha_1 = \alpha_2 = \alpha$) it follows that

$$b_1 = b_2 = \quad = -\frac{8\pi\alpha}{C_{11} + C_{12}} \tag{11}$$

The numbers to check are C_{11} and C_{12}. They are given by

$$C_{mn} = -\oint_0^2 \frac{G_n(x_m, y_m, \eta)}{(y_m - \eta)^2}\, d\eta, \tag{12}$$

where

$$G_\eta(x_m, y_m, \eta) = Y_n(\eta)\int_0^1 (1-\xi)\left[1 + \frac{x_m - \xi}{\sqrt{(x_m-\xi)^2 + \beta^2(y_m-\eta)^2}}\right] d\xi \tag{13}$$

and

$$Y(\eta) = \begin{cases} 3\eta - \frac{3}{4}\eta^2 & \eta \in S_1 = (0,1) \\ \frac{3}{4}(2-\eta)^2 & \eta \in S_2 = (1,2) \end{cases} \tag{14}$$

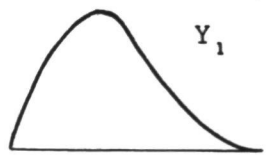

$$Y_2(\eta) = Y_1(2-\eta) \tag{15}$$

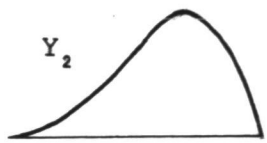

The first point of comparison between CP1 and RRX is $G(x_m,y_m,\eta)$. It may be shown that

$$G(x,y,\eta) = Y(\eta)\left[\frac{1}{2} + (1-\tfrac{1}{2}x)\sqrt{x^2+\beta^2(y-\eta)^2} - \tfrac{1}{2}(1-x)\sqrt{(1-x)^2+\beta^2(y-\eta)^2}\right.$$

$$\left. + \frac{\beta^2(y-\eta)^2}{2}\log\frac{\sqrt{(1-x)^2+\beta^2(y-\eta)^2}-(1-x)}{x+\sqrt{x^2+\beta^2(y-\eta)^2}}\right] \qquad (16)$$

where, for simplicity, the subscripts have been omitted. It is necessary to define G(x,y,y) as a limit; then

$$G(x,y,y) = \lim_{\eta \to y} G(x,y,\eta) = (2x-x^2)\,Y(\eta) \qquad (17)$$

The graph of G based on equations (16) and (17) is shown in figure 6. A small ad hoc digital computer program called ECP1 was used to calculate numerical values for all the closed-form results presented in this section. These values were then compared with the numerical values obtained by RRX. The values obtained by RRX for G were found to be accurate to about seven and one-half decimal places with an average deviation in about the eighth place. All spanwise integration stations for η were compared. A brief excerpt is shown in table 1*.

Table 1.—G(x,y,η) for x = 0.5, y = 0.5 Basis Function No. 1

η	G(x,y,η) exact	G(x,y,η) RRX	Error**, μ%
.0267 0455 5463	.5008 8328 9740 (-1)	.5008 8328 8670 (-1)	-.21
.4919 8863 3361	.6982 5165 5022	.6982 5169 2610	+3.95
.5080 1136 6639	.7072 6110 0380	.7072 6113 3184	+4.64
.9732 9544 4537	.5030 2766 2341	.5030 2766 1266	-.21
1.976 8560 5193	.2227 9916 0683 (-3)	.2227 9916 0793 (-3)	+.05

* Computations File, Runs CP1.6 and CP1.7

** One μ% error equals one part in 10^8

$$G(x,y,\eta) = \tfrac{1}{2}Y_i(\eta)\left[1 + (2-x)\sqrt{x^2+\beta^2(y-\eta)^2} - (1-x)\sqrt{(1-x)^2+\beta^2(y-\eta)^2}\right.$$

$$\left. + \beta^2(y-\eta)^2 \log \frac{\sqrt{(1-x)^2+\beta^2(y-\eta)^2} - (1-x)}{\sqrt{x^2+\beta^2(y-\eta)^2} + x}\right]$$

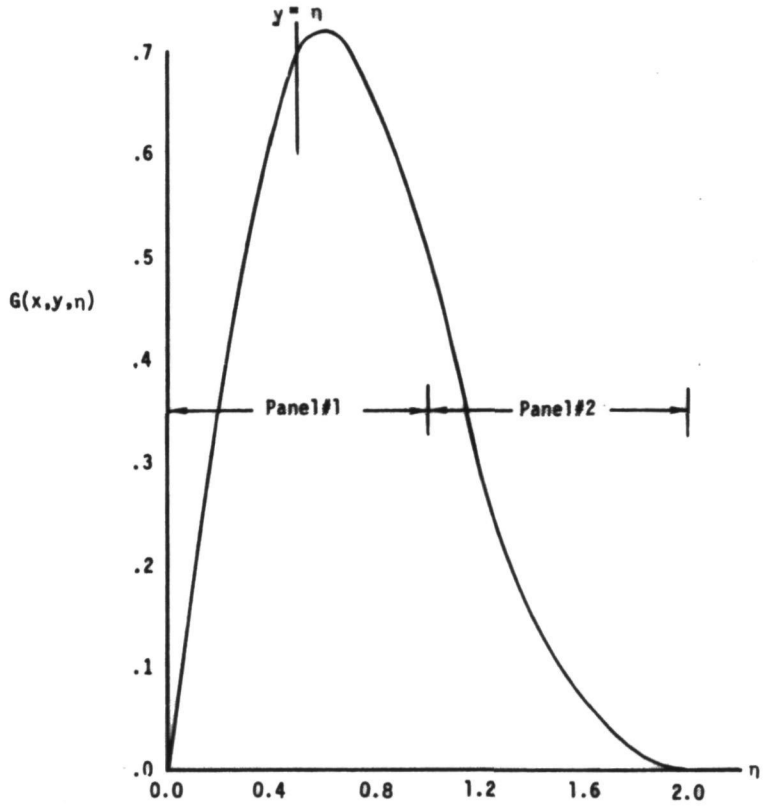

Figure 6.—Chordwise Integral-Downwash Point One (CP1)

The integrand of the spanwise integral is depicted in figure 7; it suggests clearly that the integral does not exist as an ordinary integral. Further, in order to view the effect of the G_* transformation, the graph of the singly differenced function is presented in figure 8. It may be shown that this difference function differs from its limit, the derivative $G_{,\eta}(x,y,y)$ by the order of $|y-\eta|\log|y-\eta|$ near $\eta = y$ and that an infinite slope will be exhibited in figure 8 at the point $\eta = y$ and, further, that the doubly differenced function G_* will possess a logarithmic singularity there. This singularity, which is integrable, is shown in figure 9. Removal of its logarithmic singularity is depicted in figure 10; the function $\hat{G}_*$ is completely nonsingular and hence may be easily integrated by standard, high-precision, Gaussian methods.

$$\frac{G(x,y,\eta)}{(y-\eta)^2} \sim C_{mn} = -\oint_a^b \frac{G(x,y,\eta)}{(y-\eta)^2}\, d\eta$$

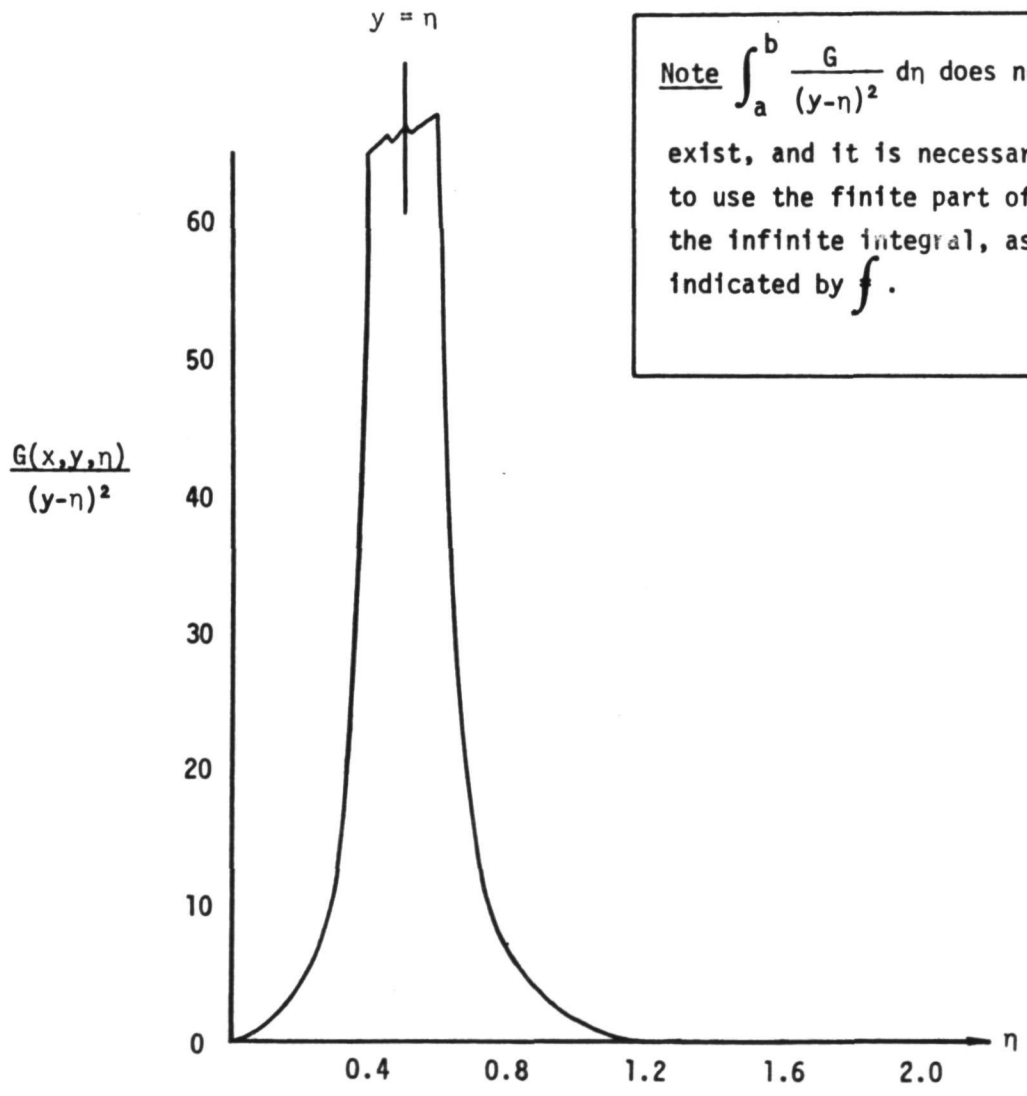

Note $\int_a^b \frac{G}{(y-\eta)^2}\, d\eta$ does not exist, and it is necessary to use the finite part of the infinite integral, as indicated by $\oint$.

Figure 7.—Integrand of the Infinite Spanwise Integral (CP1)

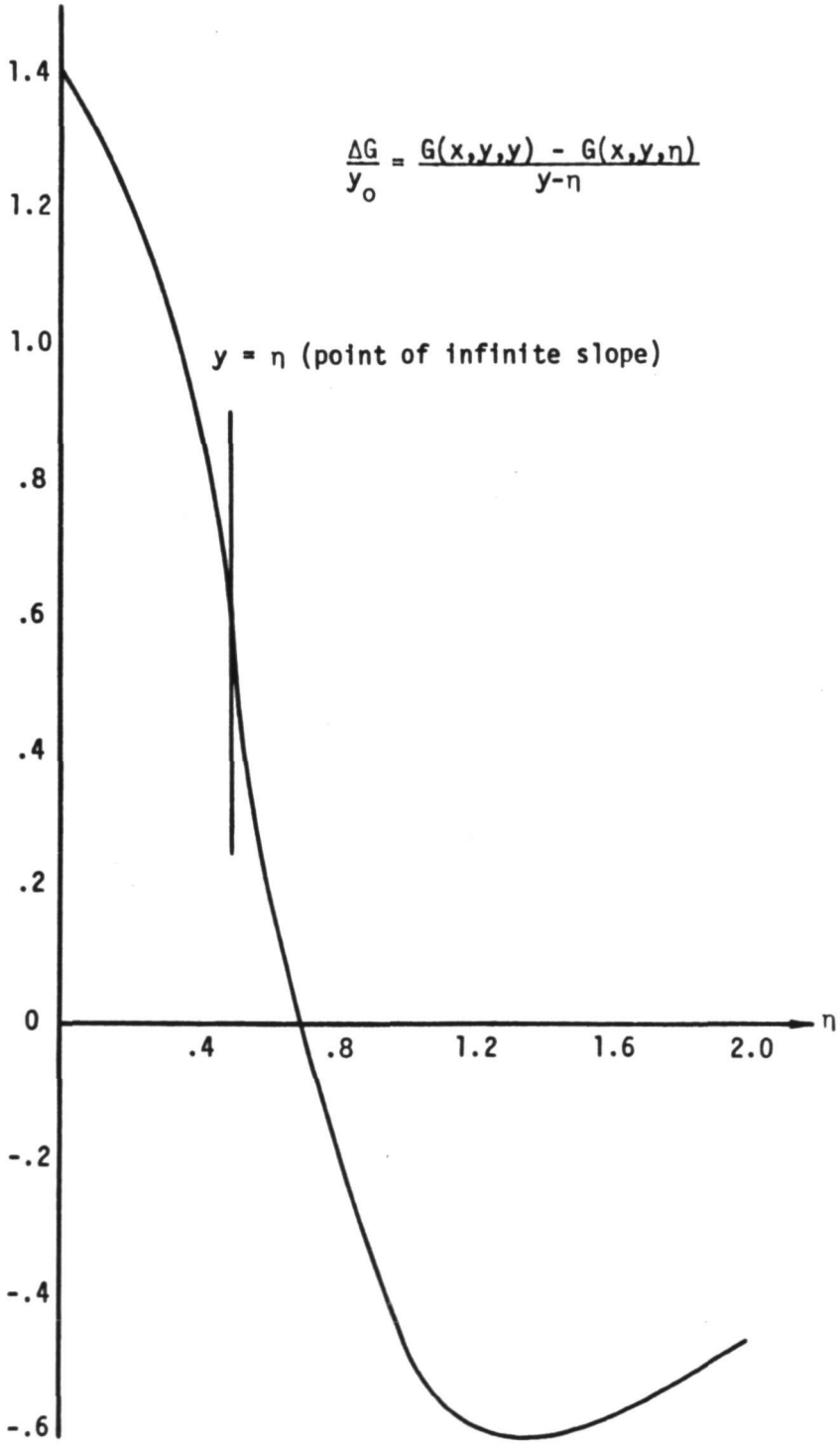

Figure 8.—Singly Differenced Spanwise Integrand (CP1)

$$G_{\star}(x,y,\eta) = \left[\frac{G(x,y,y) - G(x,y,\eta)}{y-\eta} - G_{,\eta}(x,y,y) \right] \frac{1}{y-\eta}$$

$$C_{mn} = \int_a^b G_{\star}(x,y,\eta)d\eta + G_{,\eta}(x,y,y)\log\left|\frac{y-a}{b-y}\right| + G(x,y,y)\left[\frac{1}{b-y} + \frac{1}{y-a}\right]$$

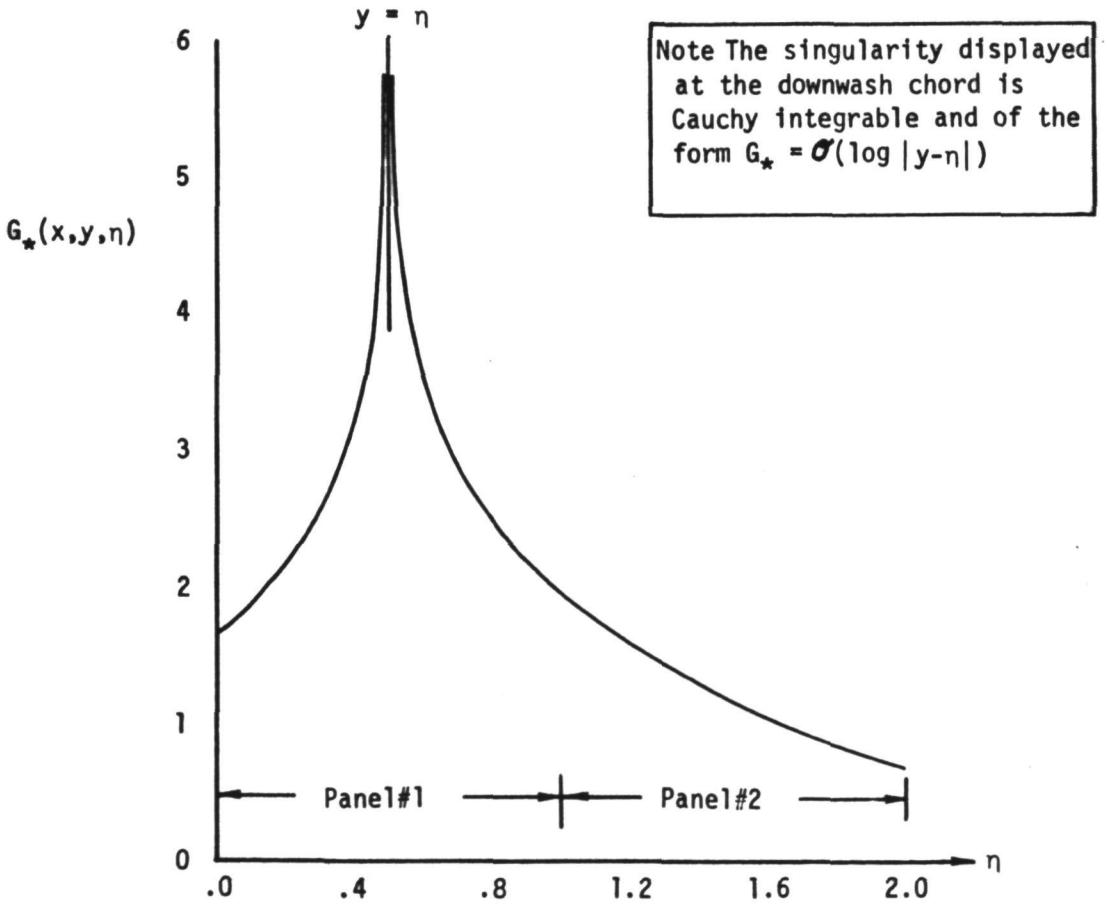

Figure 9.—Doubly Differenced Spanwise Integrand (CP1)

$$\hat{G}_{\star}(x,y,\eta) = G_{\star}(x,y,\eta) + \beta^2 Y(\eta)\log|y-\eta|$$

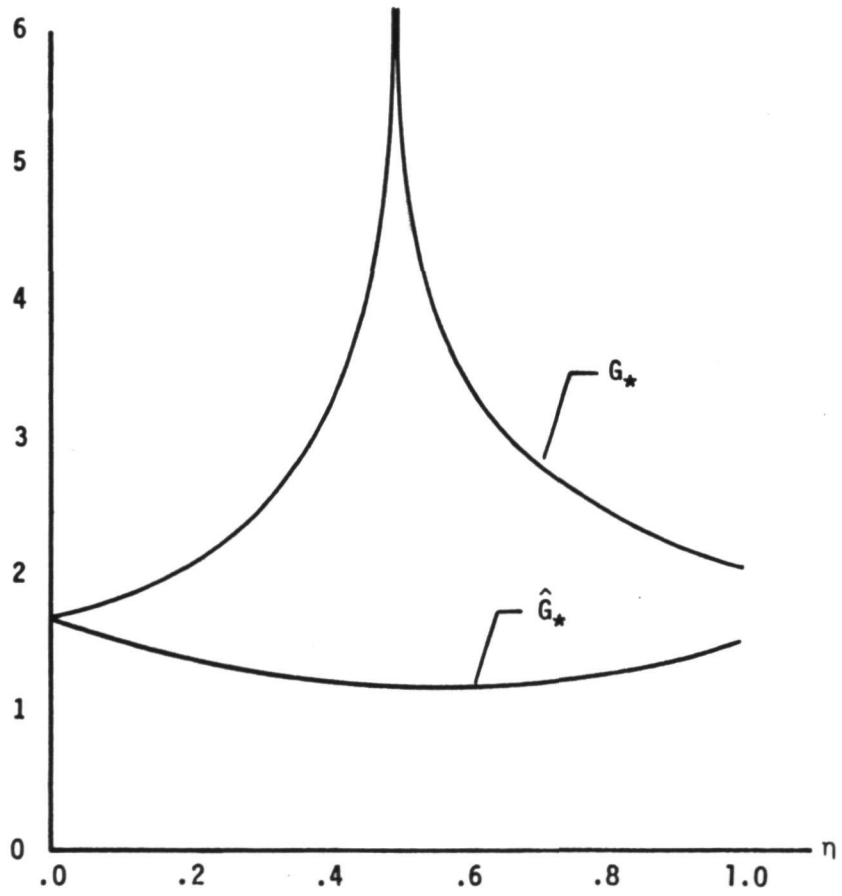

Figure 10.—Readily Integrable Spanwise Integrand (CP1)

The determination of C_{11} is made panel by panel.

$$C_{11} = -\oint_0^1 \frac{G(x,y,\eta)}{(y-\eta)^2}\, d\eta - \int_1^2 \frac{G(x,y,\eta)}{(y-\eta)^2}\, d\eta \qquad (18)$$

We consider first the integration across the second panel—that part involving the analytic integrand. From the standpoint of numerical analysis, one may use different numbers, say NG of Gaussian quadrature points, and different numbers, say NS of subintervals. These respective choices are independent, and comparative calculations were made for NG = 2,4,8,16 and NS = 1,2,4,8. The results are presented below in table 2. The 16-point single subinterval combination corresponding to NG = 16 and NS = 1 appears optimum for this case. It is clear that convergence is attained. (It may be noted that more rapid convergence may be obtained by using the doubly differenced integrand G_*.)*

Table 2.—Legendre-Gaussian Quadrature of $\int_1^2 G(x,y,\eta)/(y-\eta)^2\, d\eta$

NG	NS = 1	NS = 2	NS = 4	NS = 8
2	.2837 7825 5836	.3166 9439 1475	.3219 9429 0433	.3225 1334 6362
4	.3220 8596 6664	.3225 4332 6213	.3225 5411 7521	.3225 5422 9580
8	.3225 5420 3769	.3225 5423 0226	.3225 5423 0243	.3225 5423 0243
16	.3225 5423 0244	.3225 5423 0244	.3225 5423 0244	.3225 5423 0244

The portion of C_{11} that results from integration over the first panel,

$$-\oint_0^1 \frac{G(x,y,\eta)}{(y-\eta)^2}\, d\eta = \int_0^1 G_*(x,y,\eta)\, d\eta + G(x,y,y)\left(\frac{1}{1-y} + \frac{1}{y}\right) + G_{,\eta}(x,y,y)\log\frac{y}{1-y}\,, \qquad (19)$$

* Computations File, Run CP1.10

is for purposes of numerical integration, a matter of integrating G_* for $\eta \epsilon \left[0,1\right]$. This is conveniently done in two parts: $\eta \epsilon \left[0,y\right]$ and $\eta \epsilon \left[y,1\right]$. If one simply uses standard Legendre-Gaussian quadrature, the numerical results may be expected to be poor because of the logarithmic singularity remaining in G_* that is displayed in figure 9. This is the case, as shown in table 3. However, if in the analysis preceding numerical integration, the logarithmic singularity is separated as it is in figure 10, then Legendre-Gaussian quadratue may be used on $\hat{G}_*$ and logarithmic-Gaussian quadrature may be used on the logarithmically singular part. This is also shown in table 3. It may be seen that the eight-point Legendre-logarithmic form of Gaussian quadrature converged to almost 12 decimal places.**

Table 3.—Gaussian Quadrature of $\int_0^1 G_*(x,y,\eta)\, d\eta$

NG	Legendre Only	Legendre-logarithmic
2	2.512 6234 7443	2.770 2077 8297
4	2.582 1430 0494	2.770 0346 6808
8	2.603 6269 2847	2.770 0355 4307
16	2.609 6812 3399	2.770 0355 4308

The cumulative convergence of the numerical integration procedures for C_{mn} is shown in table 4. It is seen that the convergence is quite strong. The level of convergence is between 11 and 12 decimal places.

Table 4.—Convergence of Coefficient Matrix for CP1

NG	C_{11}	C_{12}
2	5.266 0133 9149	-.3841 4421 5347
4	5.259 9913 4187	-.3842 0916 7113
8	5.259 9813 1284	-.3842 0735 7155
16	5.259 9813 1284	-.3842 0735 7138

* Computations File, Run CP1.10
** RRX Computational File, Runs CP1.11 and CP1.13

By comparison, the results of RRX are shown in table 5 to eight decimal places. It is seen that the maximum error is 0.10% in the smaller, off-diagonal term and 0.04% in the larger and dominant diagonal terms. Because the integration procedures in RRX are rather extensively modified versions of those used in the RHO-III code, and the latter is optimized numerically for global basis functions rather than local basis functions, the agreement shown in table 5 is sufficient for our purposes.

Table 5.—Comparison of C_{mn} From RRX With Values From Table 4, Which are Essentially Exact

Source	$C_{11} = C_{22}$	$C_{12} = C_{21}$
Exact	5.259 9813	-.3842 0736
RRX	5.259 6758	-.3842 6833

Although a two-panel solution is extremely crude, it has been most interesting to compare these results with those of other codes. On the basis of the above results, it is easy to determine the basis coefficients and then to compute C_{L_α} (which is a gross measure of the ability to predict pressure accurately). This was done, and calculations were also performed (1) with the RHO-III code using 48 comparable terms (actually 24 terms per semispan), and (2) with the steady-state method of F. T. Johnson (ref. 18). The comparisons are shown in table 6. The agreement is remarkable.

Table 6.—Comparison of C_{L_α} From Different Codes

Method of Ref. 18	100 terms*	≅2.46
RHØ-III	48 terms*	2.474
RRX	2 term *	2.577

* For consistency, these are the effective numbers of terms if symmetry is not discounted; otherwise these would read 50 terms, 24 terms, and 1 term.

5.2 CHECKOUT PROBLEM TWO

The purpose of the second checkout problem, CP2, is to provide an accurate, closed-form comparison for a swept ($\Lambda_L = 45^0$), tapered ($\lambda_T = 0.5$) wing at a high subsonic Mach number ($M = 0.80$). The planform and paneling are shown in figure 11.

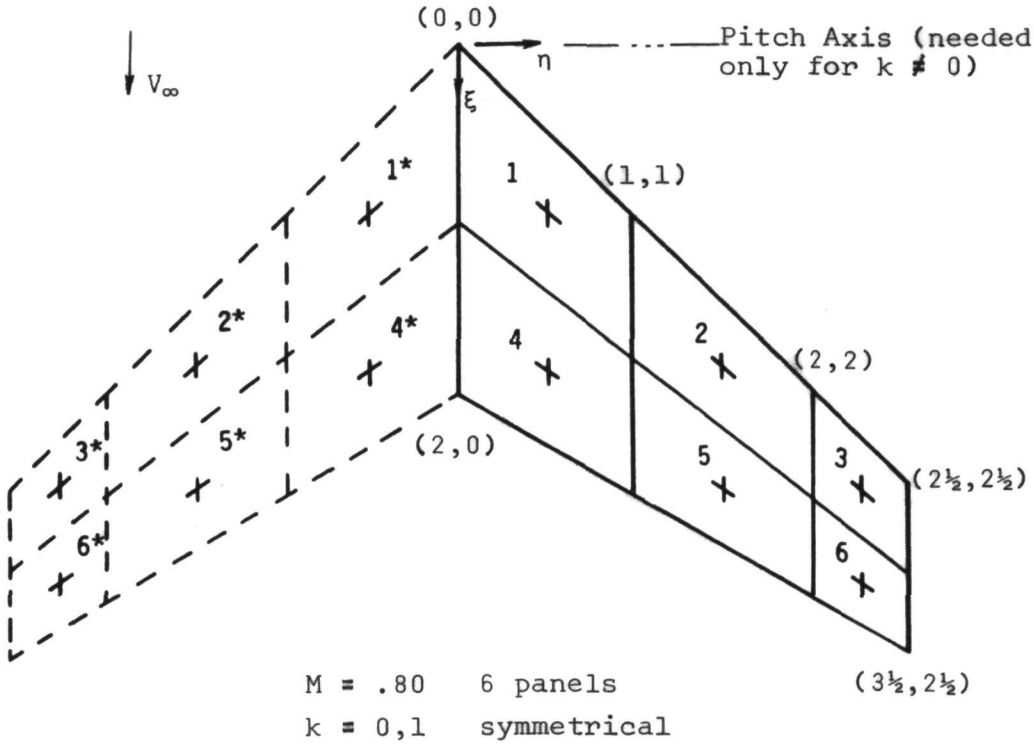

Figure 11.—Planform for Checkout Problem Two

Basis Functions: Let the functions defining the leading edge, midchord, and trailing edge, respectively, be ξ_1, ξ_2, and ξ_3. Thus,

$$\xi_1(\eta) = |\eta|, \quad \xi_2(\eta) = 1 + \frac{4}{5}|\eta| \quad \xi_3(\eta) = 2 + \frac{3}{5}|\eta|. \qquad (20)$$

The local panel coordinates are then given by*

$$(\forall\xi:\ \xi_1 \le \xi \le \xi_2)\left(\bar{\xi} = \frac{\xi - |\eta|}{1 - \frac{1}{5}|\eta|}\right) \quad \&$$

$$(\forall\xi:\ \xi_2 \le \xi \le \xi_3)\left(\bar{\xi} = \frac{\xi - 1 - \frac{4}{5}|\eta|}{1 - \frac{1}{5}|\eta|}\right) \tag{21}$$

and the functions X_μ are given by

$$(X_1 = 1-\bar{\xi}) \quad \& \quad (\xi_1 \le \xi \le \xi_2 \rightarrow X_2 = \bar{\xi}) \quad \& \quad (\xi_2 \le \xi \le \xi_3 \rightarrow X_2 = 1-\bar{\xi}). \tag{22}$$

The streamwise functions, X_μ, are depicted generically in figure 2. For this particular problem, the spanwise functions, Y_ν, are depicted by figure 12.

$$(0 \le \eta \le 1 \rightarrow Y_1 = 1 - \tfrac{1}{2}\eta^2) \ \& \ (1 \le \eta \le 2 \rightarrow Y_1 = \tfrac{1}{2}(2-\eta)^2) \tag{23}$$

$$(0 \le \eta \le 1 \rightarrow Y_2 = \tfrac{7}{10}\eta^2) \ \& \ (1 \le \eta \le 2 \rightarrow Y_2 = \tfrac{7}{30}(-10+20\eta-7\eta^2))$$

$$\& \ (2 \le \eta \le 2\tfrac{1}{2} \rightarrow Y_2 = \tfrac{7}{15}(5-2\eta)^2) \tag{24}$$

$$(1 \le \eta \le 2 \rightarrow Y_3 = \tfrac{8}{9}(\eta-1)^2) \ \& \ (2 \le \eta \le 2\tfrac{1}{2} \rightarrow Y_3 = 1 - [1-\tfrac{4}{3}(5-2\eta)^2]) \tag{25}$$

Chordwise Integrals: For simplicity, the indices n and m for basis function and downwash point, respectively, are frequently omitted below; however, it should be clear from the context what is meant.

The chordwise integrals are given by

$$G(x,y,\eta) = Y(\eta) \int_{\{\xi:\, p(\xi,\eta)\neq 0\}} X(\bar{\xi})\ \mu(x-\xi, y-\eta)\, d\xi, \tag{26}$$

*The symbolism $(\forall\xi{:}P)\ (Q)$ means for every ξ satisfying P, then ξ also satisfies Q.

where

$$\mu(x-\xi, y-\eta) = 1 + \frac{x - \xi}{\sqrt{(x-\xi)^2 + \beta^2(y-\eta)^2}} \qquad (27)$$

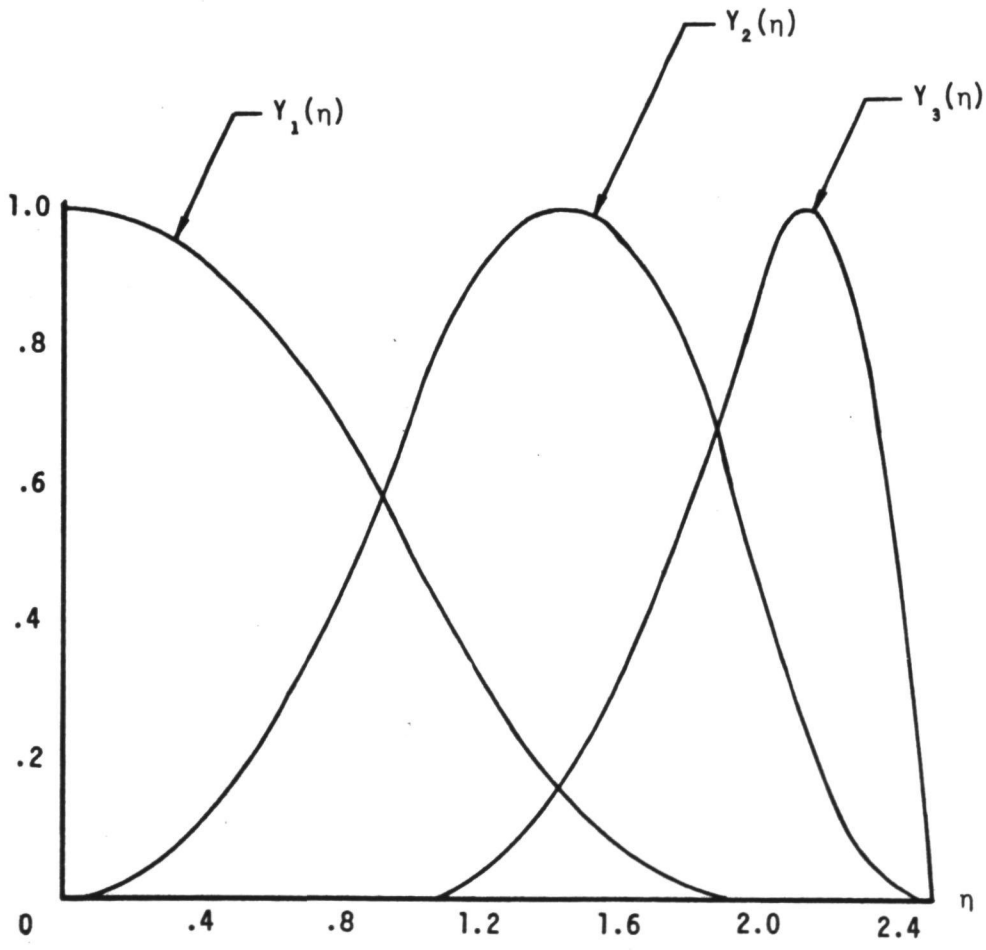

Figure 12.—Spanwise Spline Functions (CP2)

Since $X(\bar{\xi})$ is linear in $X-\xi$, G is expressible in terms of the indefinite integrals

$$\phi(x-\xi,y-\eta) = \int \mu(x-\xi,y-\eta)d\xi \tag{28}$$

$$\psi(x-\xi,y-\eta) = \int (x-\xi)\mu(x-\xi,y-\eta)d\xi, \tag{29}$$

and one finds

$$\phi(x-\xi,y-\eta) = -(x-\xi) - \sqrt{(x-\xi)^2 + \beta^2(y-\eta)^2}\ , \tag{30}$$

$$\psi(x-\xi,y-\eta) = -\tfrac{1}{2}(x-\xi)^2 - \tfrac{1}{2}(x-\xi)\sqrt{(x-\xi)^2 + \beta^2(y-\eta)^2}$$
$$+ \tfrac{1}{2}\beta^2(y-\eta)^2\log\left[\sqrt{(x-\xi)^2 + \beta^2(y-\eta)^2} + (x-\xi)\right] \tag{31}$$

Indeterminacies in ϕ and ψ must be handled as limits. In addition, it is essential to recognize that along $\eta = y$, the behavior of certain singularities* depends only upon the sign of $x-\xi$. One finds

$$G(x,y,\eta) = \frac{\Gamma(\eta)}{c(\eta)}\Big\{[\xi_2(\eta)-x][\phi(x-\xi_2(\eta),y-\eta) - \phi(x-\xi_1(\eta),y-\eta)]$$

$$(\forall n: 1\le n\le 3) \qquad + [\psi(x-\xi_2(\eta),y-\eta) - \psi(x-\xi_1(\eta),y-\eta)]\Big\}\ , \tag{32}$$

$$G(x,y,\eta) = \frac{\Gamma(\eta)}{c(\eta)}\Big\{[\xi_3(\eta)-x][\phi(x-\xi_3(\eta),y-\eta) - \phi(x-\xi_2(\eta),y-\eta)]$$

$$(\forall n: 4\le n\le 6) \qquad + [\psi(x-\xi_3(\eta),y-\eta) - \psi(x-\xi_2(\eta),y-\eta)]$$

$$+ [x-\xi_1(\eta)][\phi(x-\xi_2(\eta),y-\eta) - \phi(x-\xi_1(\eta),y-\eta)]$$

$$- [\psi(x-\xi_2(\eta),y-\eta) - \psi(x-\xi_1(\eta),y-\eta)]\Big\}\ , \tag{33}$$

*In order to calculate $G(x,y,\eta)$ or $G_{,\eta}(x,y,y)$, the streamwise locations of the downwash coordinate x with respect to the panel boundaries ξ_1, ξ_2, ξ_3 enter via the signs of $x-\xi_1(\eta)$, $x-\xi_2(\eta)$, and $x-\xi_3(\eta)$.

where $c(\eta)$ is the local panel chord.

Based on the above closed-form expressions, the values of $G(x,y,\eta)$, $G(x,y,y)$, and $G_{,\eta}(x,y,y)$ were computed* with an ad hoc digital computer program called ECP2. Computations were made at each downwash point and at each of the many spanwise integration stations used by RRX. Several thousand numbers were compared;** the results of RRX for the CP2 were as accurate as in CP1.

For this problem, C_{mn} will depend upon integration over as many as 12 panels. The downwash point will belong to, at most, one panel, and the Hadamard integral must be performed for that particular panel. All other panels support analytic integrands. Thus, we may write

$$C_{mn} = \sum_{(a<y<b)} \left[\int_a^b \frac{G(x,,,\eta)}{(y-\eta)^2}\, d\eta \right] + \int_{a_*}^{b_*} G_*(x,y,\eta)\, d\eta$$

$$+ G(x,y,y)\left[\frac{1}{b_*-y} + \frac{1}{y-a_*}\right] + G_{,\eta}(x,y,y) \log \frac{y-a_*}{b_*-y} \,, \qquad (34)$$

where the summation is performed over the spanwise coordinate projection of those panels in which the downwash point is not contained, and the last three terms correspond to the one in which it is. The analytic integrands on the intervals integrated by ordinary Legendre-Gaussian quadrature and the logarithmically singular integrands on $[a_*,b_*]$ are integrated by logarithmic-Gaussian quadrature. On the basis of these calculations,*** the 6 x 6 coefficient matrix for CP2 is shown to six decimal places. Values from RRX are shown in parentheses below the exact values.

*Values of G and $G_{,\eta}$ along $\eta = y$ must be worked out analytically from the above expressions due to indeterminacies. Limit calculations on the computer using ECP2 were fatally ill conditioned.

**RRX Calculations File, Runs CP2.3 through CP2.9.

***RRX Calculations File, Runs CP2.10 through CP2.14. The results converged to 11 decimal places.

$$[C_{mn}] = \begin{bmatrix} 2.41\ 405 & .729\ 411 & -.034\ 795 & -1.76\ 993 & .066\ 543 & -.044\ 384 \\ (2.41\ 419) & (.729\ 438) & (-.034\ 795) & (-1.76\ 961) & (.066\ 607 & (-.044\ 384) \\ -1.23\ 159 & 3.58\ 102 & 1.12\ 170 & -2.26\ 456 & -1.58\ 112 & .186\ 115 \\ (-1.23\ 161) & (3.58\ 089) & (1.12\ 167) & (-2.26\ 454) & (-1.58\ 098) & (.186\ 145) \\ -.465\ 187 & -1.86\ 858 & 3.41\ 598 & -.822\ 622 & -2.80\ 607 & -1.63\ 181 \\ (-.465\ 187) & (-1.86\ 860) & (3.41\ 585) & (-.822\ 621) & (-2.80\ 606) & (-1.63\ 169) \\ 2.23\ 192 & -.679\ 055 & -.119\ 257 & 4.69\ 607 & .028\ 633 & -.139\ 504 \\ (2.23\ 192) & (-.679\ 013) & (-.119\ 219) & (4.69\ 620) & (.028\ 760) & (-.139\ 504) \\ -1.13\ 757 & 3.40\ 261 & -.108\ 931 & -2.27\ 143 & 6.95\ 942 & .964\ 842 \\ (-1.13\ 757) & (3.40\ 261) & (-.108\ 930) & (-2.27\ 145) & (6.95\ 929) & (.964\ 812) \\ -.483\ 378 & -1.75\ 293 & 4.63\ 633 & -.924\ 643 & -3.49\ 212 & 8.13\ 560 \\ (-.483\ 378) & (-1.75\ 293) & (4.63\ 633) & (-.924\ 643) & (-3.49\ 214) & (8.13\ 547) \end{bmatrix}$$

In addition, the pressure basis function coefficients are

$$[b_n] = \begin{matrix} [9.68\ 476 & 8.25\ 933 & 14.8471 & 2.25\ 404 & 2.36\ 621 & -1.74\ 502] \\ (9.68\ 387) & (8.25\ 935) & (14.8476) & (2.25\ 420 & (2.36\ 619) & (-1.74\ 532) \end{matrix},$$

and the total lift and center of pressure are

$$C_{L_\alpha} = 3.74\ 249 \quad (3.74\ 241),$$

$$\overline{X}_{cp} = .252\ 220 \quad (.252\ 224),$$

$$\overline{\eta}_{cp} = .432\ 977 \quad (.432\ 980).$$

The RHO-III code was used again to compute C_{L_α} for CP2 and the results are within 1% of RRX.

$$C_{L_\alpha} = 3.742 \quad \text{(RHØ-III using 24 terms)}$$

$$C_{L_\alpha} = 3.784 \quad \text{(RAMROD-X using 6 terms)}$$

This agreement is very good in view of the fact that the six-panel representation is quite crude. Since there are only two streamwise rows of panels, the chordwise pressure distribution consists of exactly two straight lines. This representation is illustrated in figure 13. Although no comparison of pressure was made with the RHO-III code, the sectional lift and center of pressure were compared and the results are shown in figure 14. The agreement for sectional distributions is quite good, but not as good as that of the lift coefficient. In general, integrated coefficients agree most closely and are the least severe comparison, sectional distributions tend to agree less closely and are a more severe comparison, and pressure comparisons are the most severe of all.

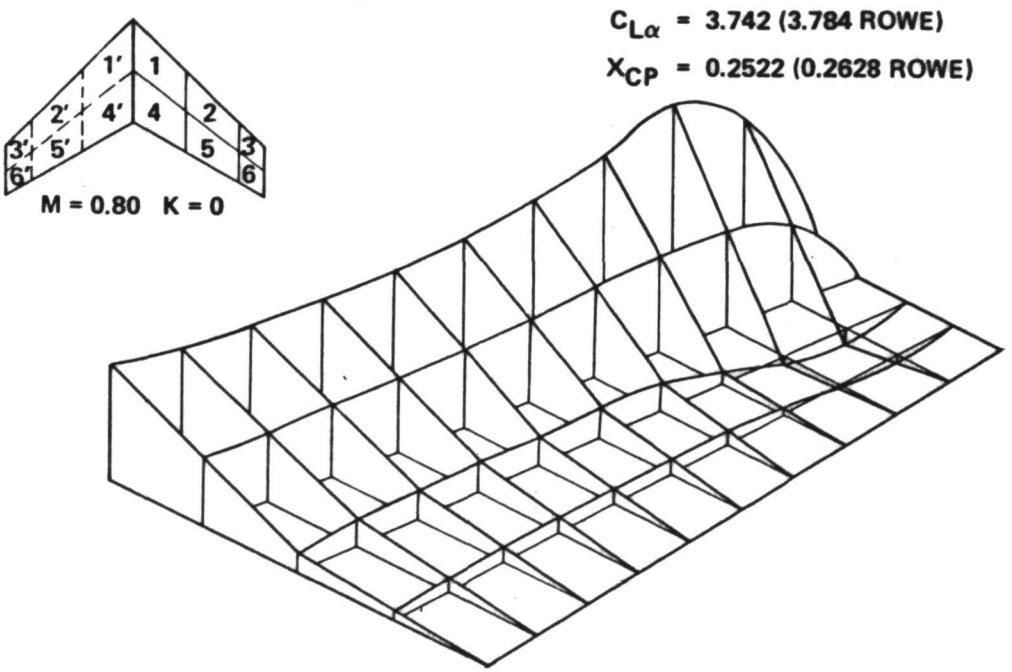

Figure 13.—Pressure Distribution From a Small Number of Basis Functions

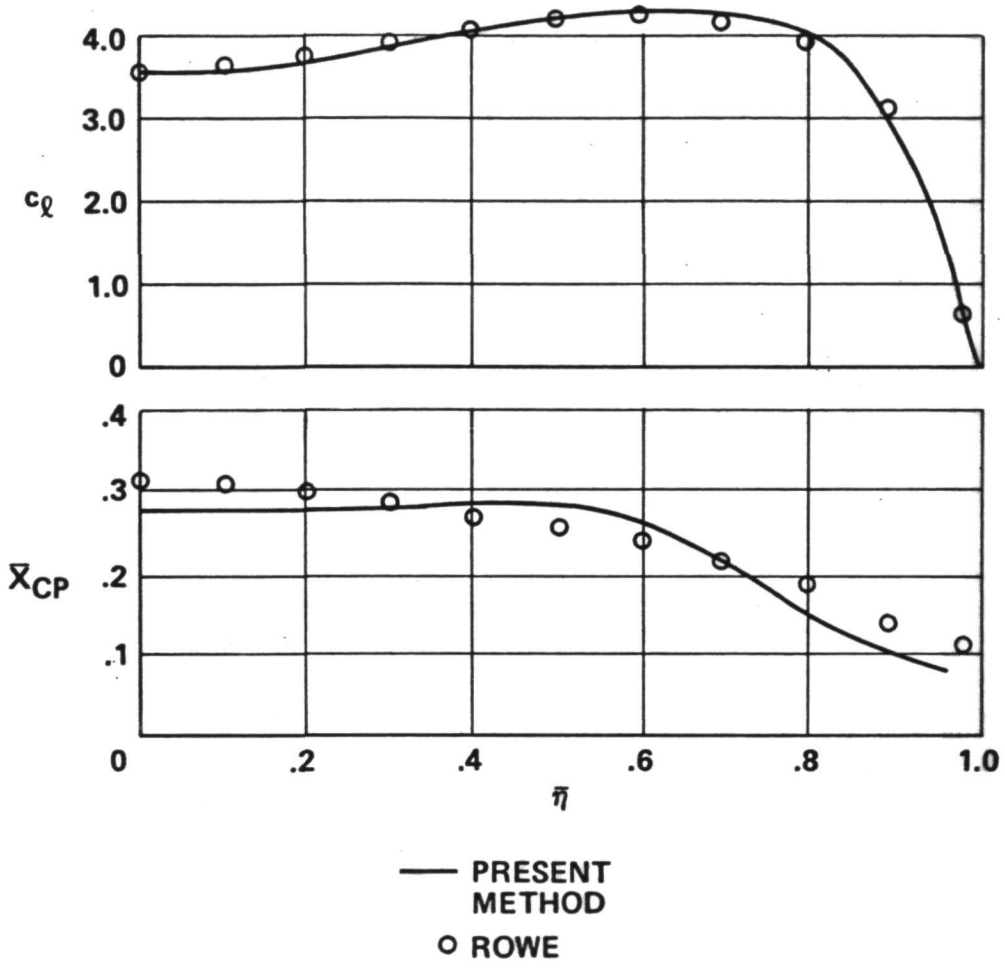

Figure 14.—Sectional Distributions From a Small Number of Basis Functions

5.3 VALIDATION PROBLEM ONE

The purpose of the first validation problem, VP1, is to validate the code for an unsteady problem by: (1) evaluating the numerical convergence characteristics as the norm of the support is decreased, and (2) comparing the results with those from another code of recognized reliability and accuracy. The planform selected is the same as that of CP2. The downwash mode is rigid uniform pitch about the apex.

In this particular study, all unsteady calculations are compared with the results of the RHO-III code. This code was adopted in 1968 by AGARD as their primary standard for unsteady aerodynamics.

Calculations for VP1 are arranged into four series: the CP2 series, A series, B series, and C series.

CP2 Series: The first nonsteady run made with RRX was the same as CP2 except with the reduced frequency set equal to unity. Whereas for the steady-state case (k = 0), the error in C_{L_α} was 1%; in the unsteady case (k = 1), the error was 22%.* The extent of this change is indicative of the difficulties encountered as one passes from steady to unsteady flow.

The first question addressed is what are the improvements that are gained by increasing the number of panels. It would be natural to expect a greater improvement from increasing the number of chordwise panels than from an equivalent increase in the number of spanwise panels. Therefore, the second run used four chordwise panels instead of only two. This caused the error to drop from 22% to 7%.

The results of the lift coefficient calculations are depicted in figure 15 using the complex plane representation. The comparison for the steady-state calculations is shown also, appearing along the real axis. The panel arrangements are indicated as the number of chordwise panels times the number of spanwise panels. Thus, for example, 4C x 3S indicates four chordwise panels and three spanwise panels. This same representation is used for the RHO-III calculations, but in that case, 6C x 4S denotes six chordwise pressure functions by four spanwise pressure functions. For the six-panel calculations, the sectional distributions for lift coefficient and center of pressure are compared in figure 16 with the 24 term results from RHO-III. The agreement is seen to be quantitatively fair and qualitatively correct. Additional comparisons, using more panels, will be presented later (C series).

*For purposes of the present study, error is defined in the unsteady case as the magnitude of the complex difference between the RRX and RHO-III values, divided by the RHO-III value.

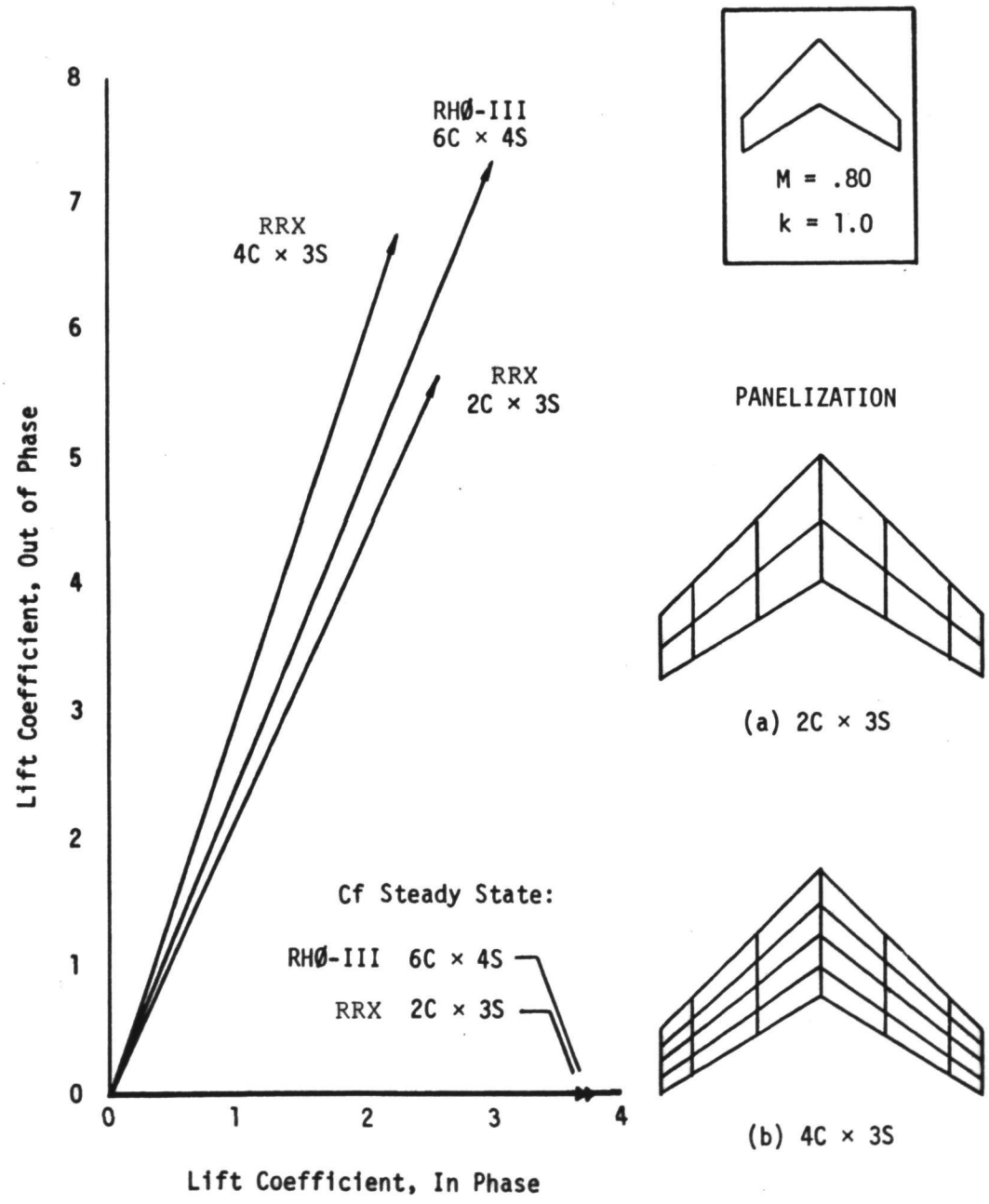

Figure 15.—Nonsteady Lift Convergence—Validation Problem One (CP2 Series)

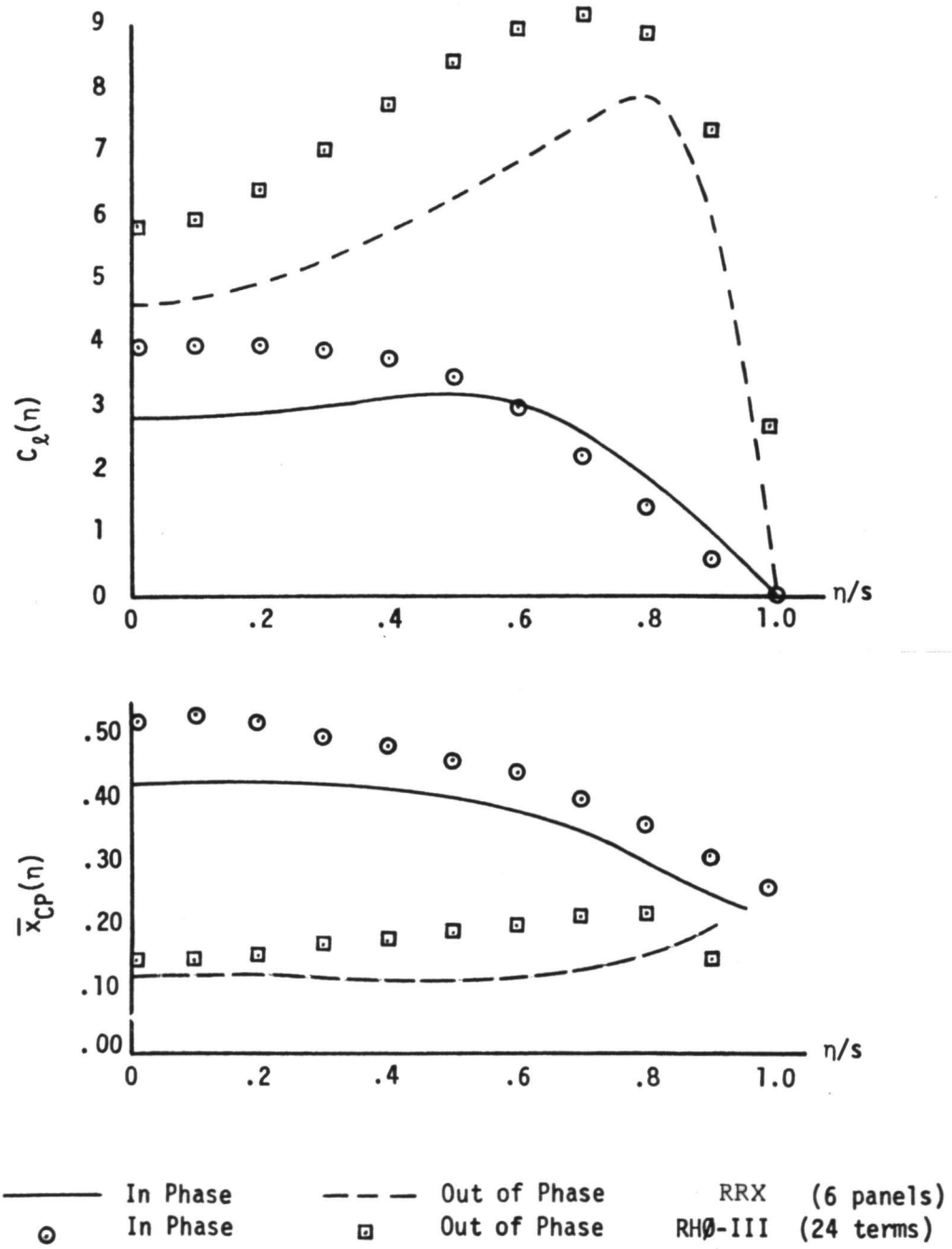

Figure 16.—Comparison of Nonsteady Sectional Distributions for Six Panels—VP1 (CP2 Series)

A Series: The purpose of this series is to study the convergence of C_{L_α} as the panels are made smaller, first in the spanwise direction, then in the chordwise direction, then both.

Four panelizations are employed 2C x 2S, 2C x 4S, 4C x 2S, and 4C x 4S. Having no a priori panelization criteria for the RRX code, we begin by using in this series the so-called Multhopp equiangular partition (ref. 19) in which the chordwise and spanwise panel boundaries are determined by

$$\bar{X} = \frac{1 - \cos\theta}{2} \qquad 0 \leq \theta \leq \pi \tag{35}$$

$$\bar{\eta} = \cos\phi \qquad 0 \leq \phi \leq \pi/2 \tag{36}$$

where equal angular increments in θ and ϕ are used. The effect is to increase the panel density in the regions of largest pressure gradients; i.e., along the leading and trailing edges (where the pressure gradient is infinite) and along the tip (where it is also infinite). These panelizations are illustrated in figure 17.

By and large, the results are as expected. The 2C x 2S run produced an error in C_{L_α} of 21.2%. Doubling the number of spanwise panels produced an error of 21.5% but with a more accurate phase angle, as may be seen by referring to figure 18. On the other hand, doubling instead the number of chordwise panels reduced the error to 5.4%. It is apparent that in the present method, it is preferable to have a larger number of chordwise panels than spanwise panels. Finally, doubling both the number of chordwise and spanwise panels reduced the error even further to 3.5%. It may be observed that the 4C x 4S case has nearly the same magnitude as the 4C x 2S case, but that the 4C x 4S case has a more accurate phase angle, an important criterion in problems such as flutter, and is an effect that the complex error magnitude criterion may not accurately reflect. In any event, however, it is clear that this series does display positive convergence characteristics.

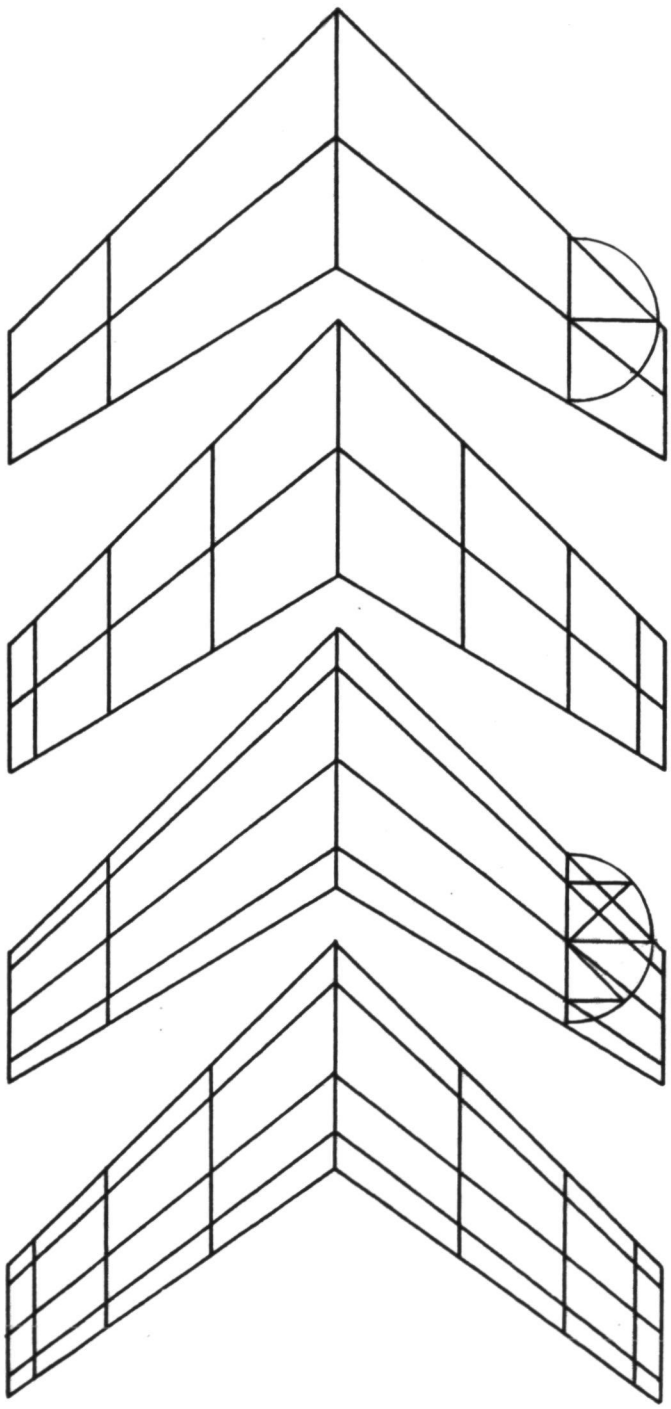

Figure 17.—Equiangular Panelization—VP1 (A Series)

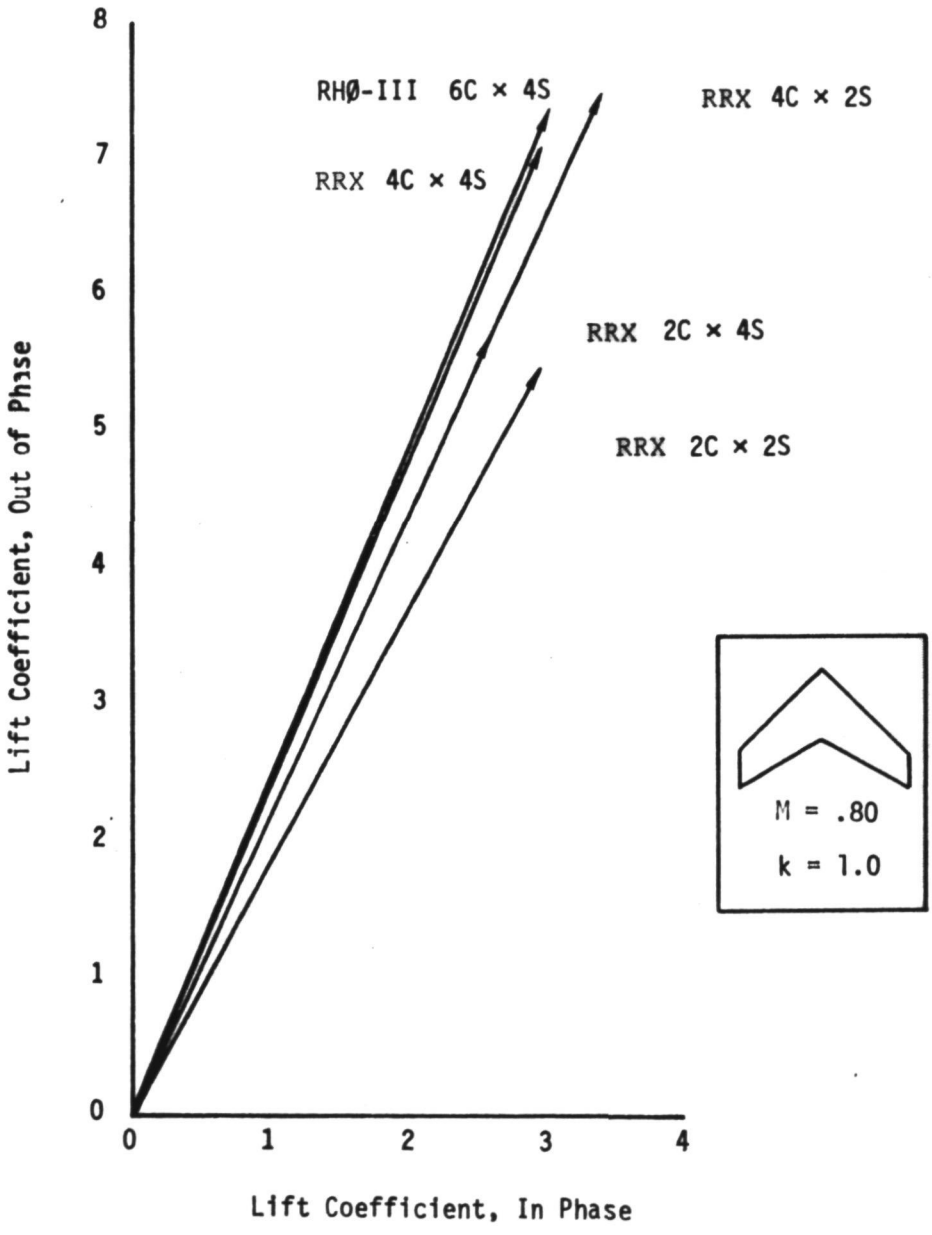

Figure 18.—Nonsteady Lift Convergence for Equiangular Panelization—VP1 (A Series)

B Series: The purpose of this series is to investigate the solution sensitivity of the RRX code to panelization density in terms of accuracy and convergence as compared with the A series of calculations.

The panelizations are again 2C x 2C, 2C x 4S, 4C x 2S, and 4C x 4S. In this series, however, panel boundaries are equidistant, as illustrated in figure 19. From a practical viewpoint, equidistant panelization has certain advantages of simplicity over the equiangular panelization. Ideally, it would be hoped that the solution is relatively insensitive to the particular panelization. Referring to figure 20, this is apparently the case, with a slight deterioration in accuracy (≈1%) when the equidistant panelization is used. In particular, 2C x 2S has an error in C_{L_α} of 22.4%, the 2C x 4S of 22.5%, the 4C x 2S of 6.9%, and 4C x 4S of 9.2%.

The fact that the 4C x 4S panelization is less accurate than the 4C x 2S is anomalous. Once this anomaly is recognized, it is seen to be present in the 2C x 4S (22.5%) and 2C x 2S (22.4%) pair, though to a lesser extent. In retrospect, it was also present in the A series: compare 2C x 4S (21.5%) with 2C x 2S (21.2%). The spanwise panel widths near the root are much narrower in the equidistant case than in the equiangular case. Since the collocation points are being placed at midpanel,* it is seen that, with equidistant spacing, the distance from the apex chord to the inner collocation points is much closer than with the equiangular spacing. Since the apex induces a singularity in downwash that is physically inadmissible and erroneous, placing collocation points close to such a singularity will produce erroneous results. Further, the Küssner operator is known to be discontinuous for planforms with breaks. It is apparent that to avoid placing unnecessary restrictions on the location of collocation points, the planform must be smoothed, and the smoothing must, in practice, be applied to the interior panel boundaries as well.

C Series: The purpose of the C series of calculations is to refine the panelization further and to examine the convergence of the pressure distribution.

The convergence of C_{L_α} may be seen at a glance from figure 21. Using 4, 16, and 64 panels, the errors are 21.2%, 3.5%, and 1.5%, respectively. The next level of comparison is that of the sectional distributions, shown in figure 22. It is seen that the results converge to the results of the RHO-III code except near the root in the vicinity of the apex singularity. The most severe level of comparison is that of the actual pressure distribution. This is shown in figures 23, 24, and 25 for 4, 16, and 64 panels, respectively, for the mid-semispan chord. For a preliminary study, the convergence may be considered quite good. The approximational limitations imposed by chordwise linearity of the basis functions also may be seen.

*This is a choice of expediency, not a necessity. In fact, the control points need not be in each and every panel, and some panels may have more than one control point. The *only* requirements are that the number of control points equal or exceed the number of panels ($N_w \geq N_b$), and that the control points do not lie exactly on the boundary of any panel (otherwise equation (7) does not hold).

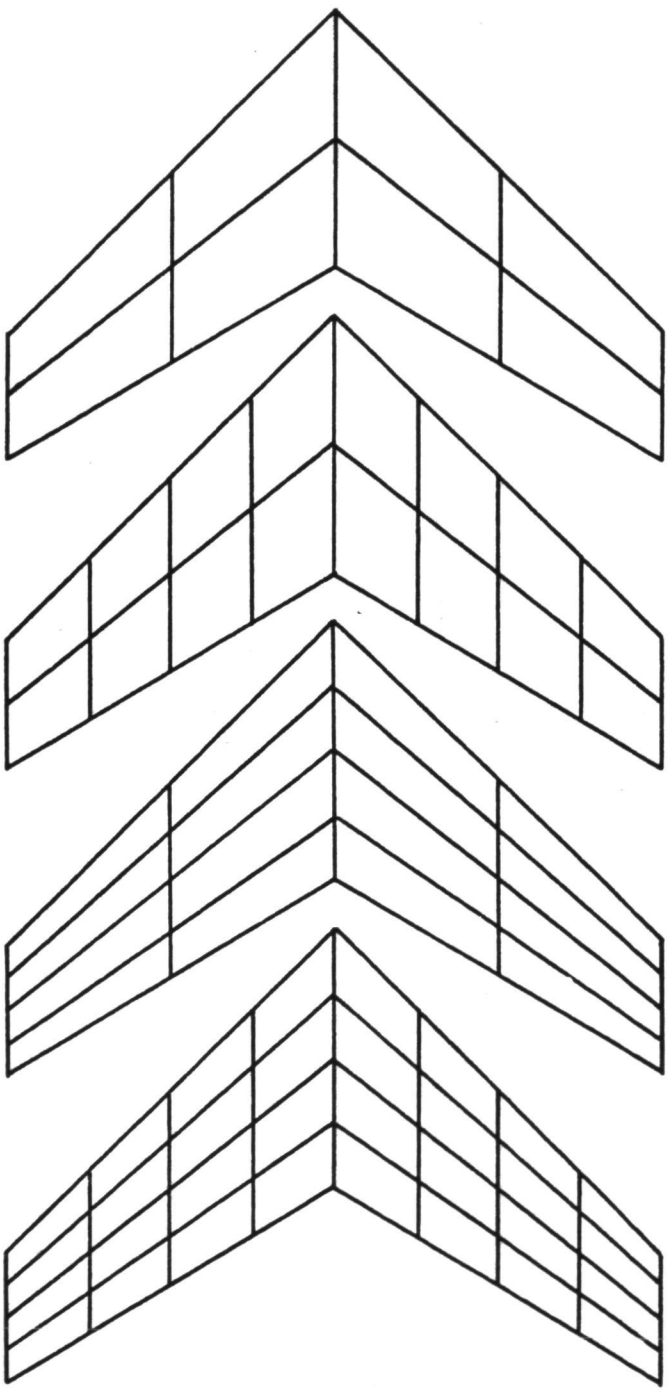

Figure 19.—Equidistant Panelization—VP1 (B Series)

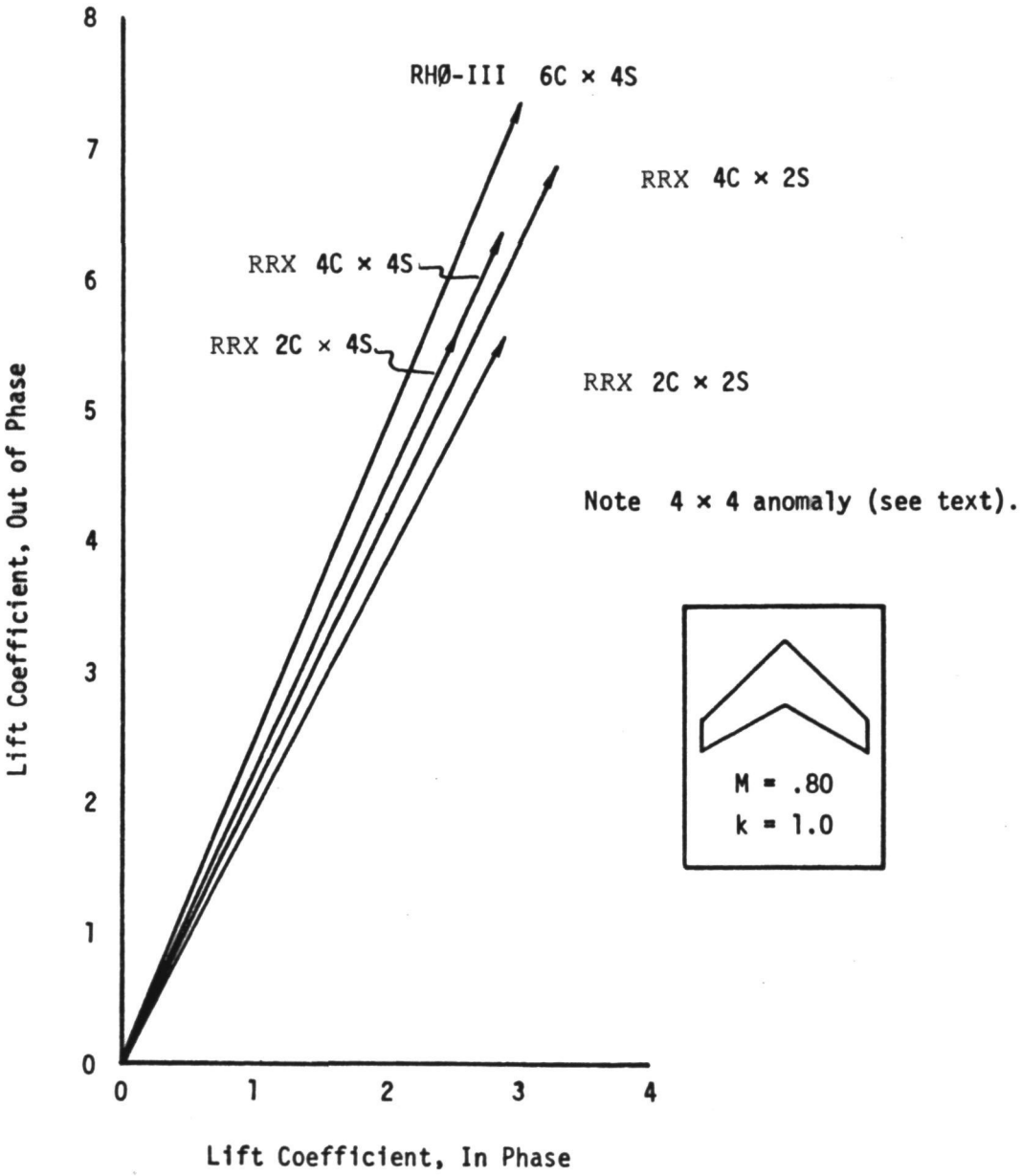

Figure 20.—Nonsteady Lift Convergence for Equidistant Panelization—VP1 (B Series)

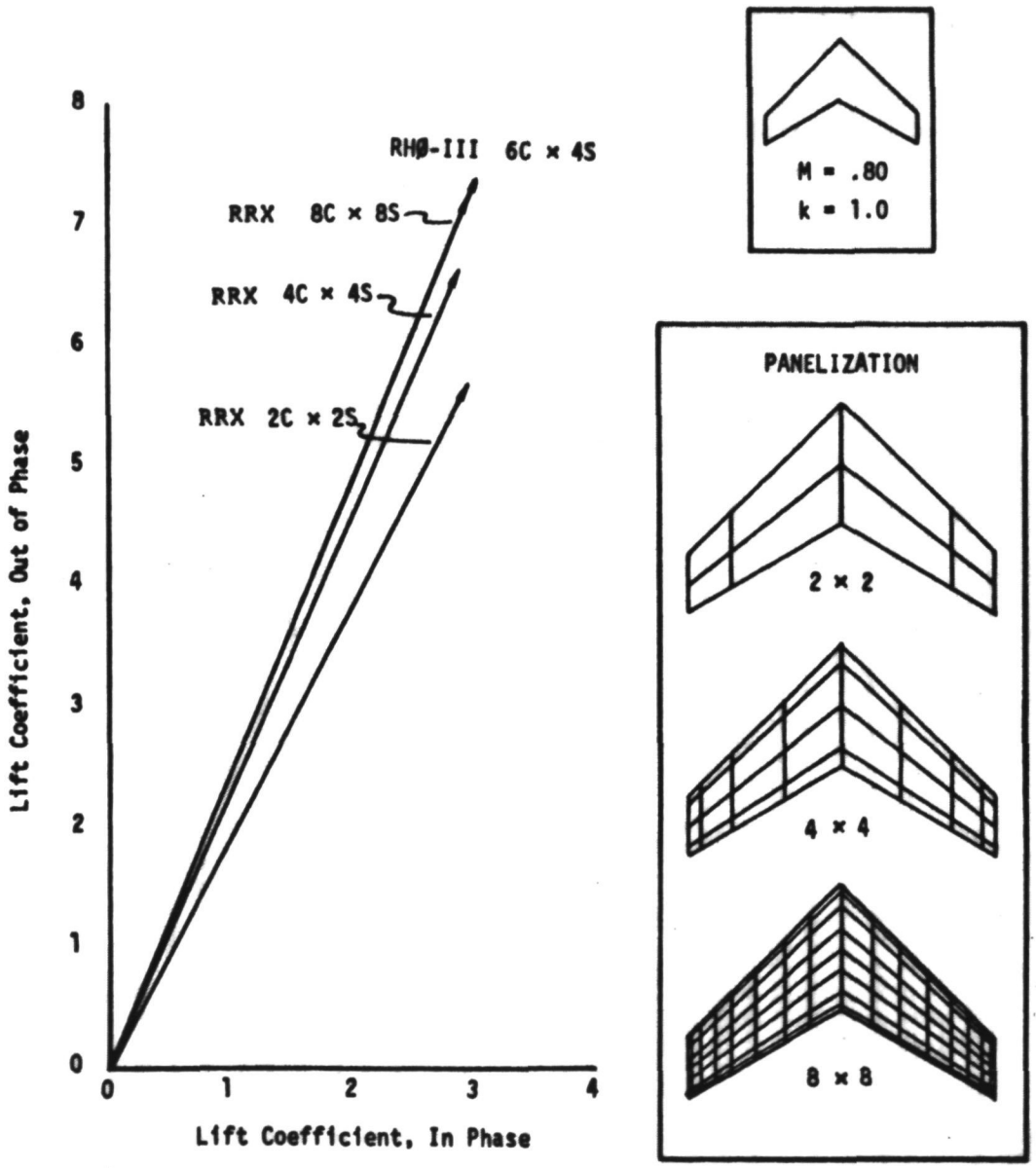

Figure 21.—Nonsteady Lift Convergence for 4, 16, and 64 Panels—VP1 (C Series)

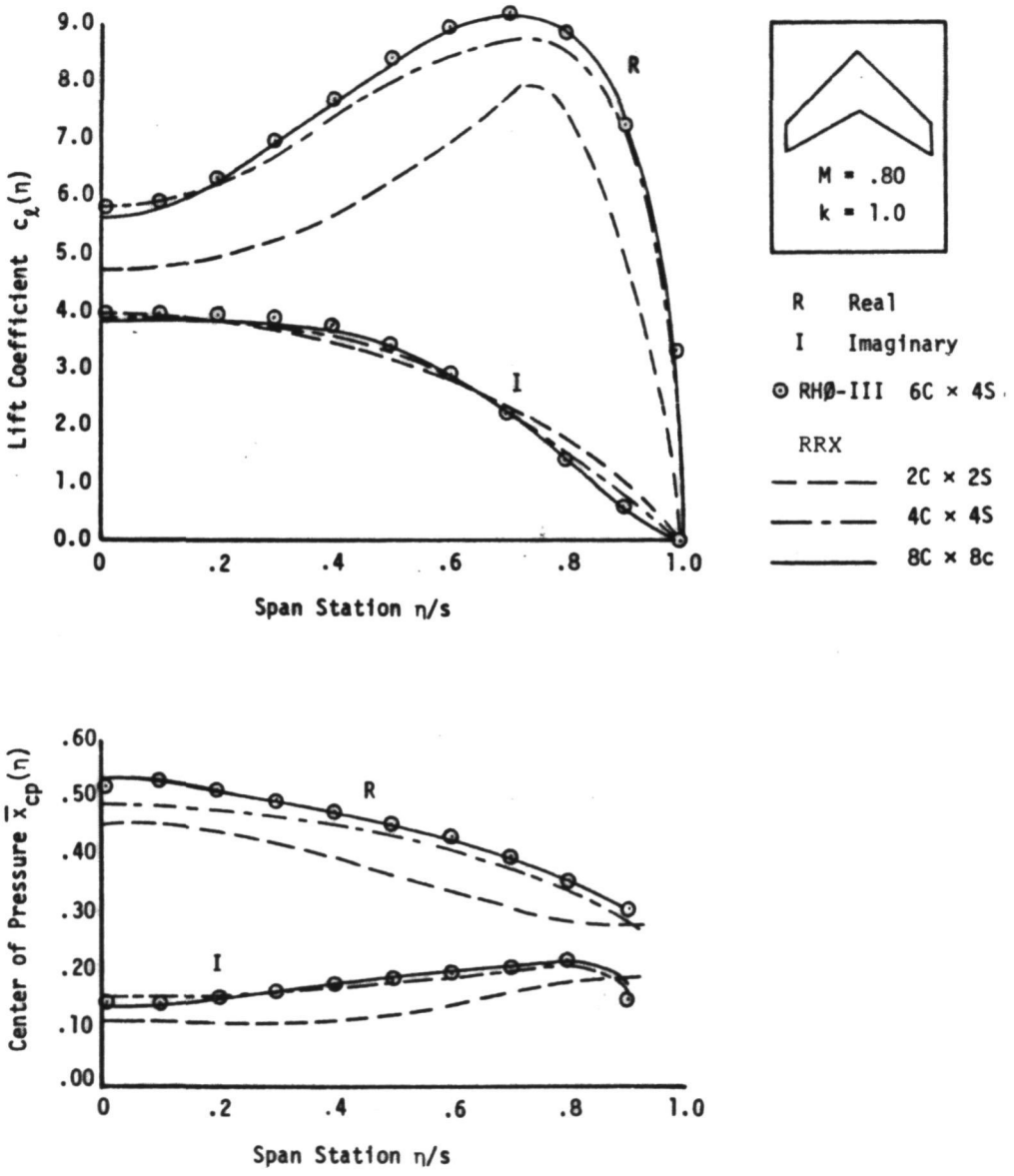

Figure 22.—Nonsteady Section Loads Convergence Using 4, 16, and 64 Panels—VP1 (C Series)

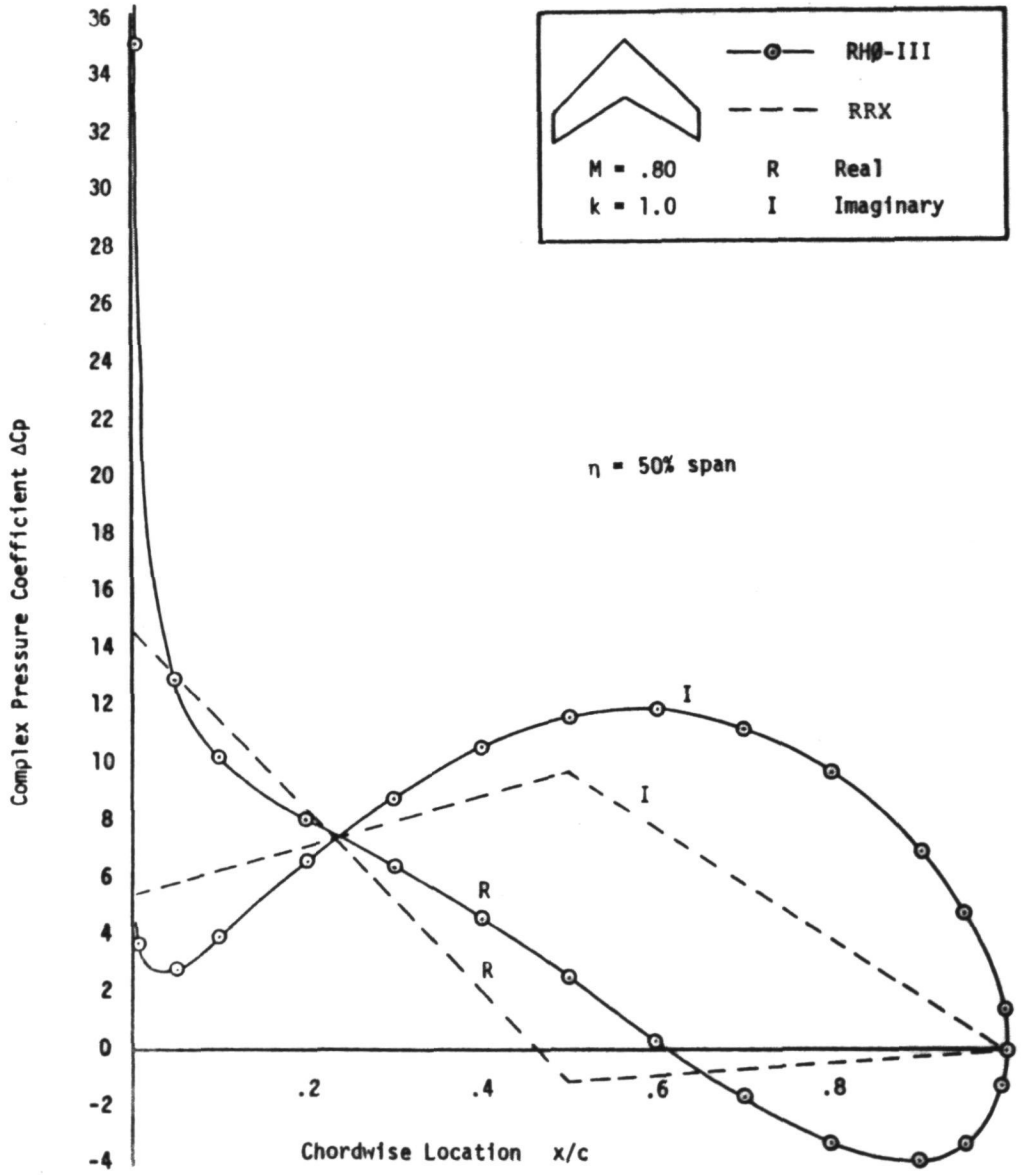

Figure 23.—Comparison of Nonsteady Pressure Using Two Chordwise Panels—VP1 (C Series)

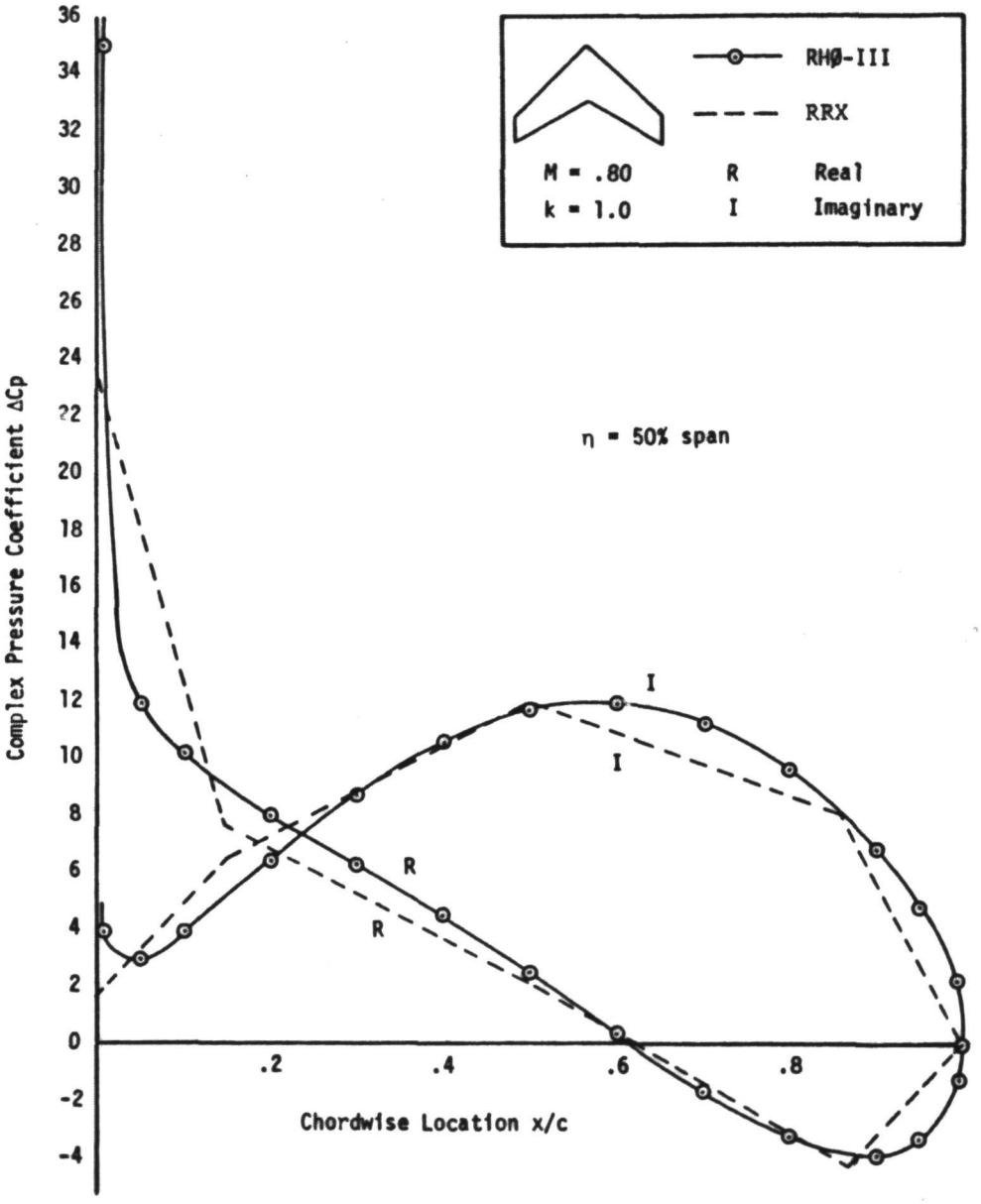

Figure 24.—Comparison of Nonsteady Pressure Using Four Chordwise Panels—VP1 (C Series)

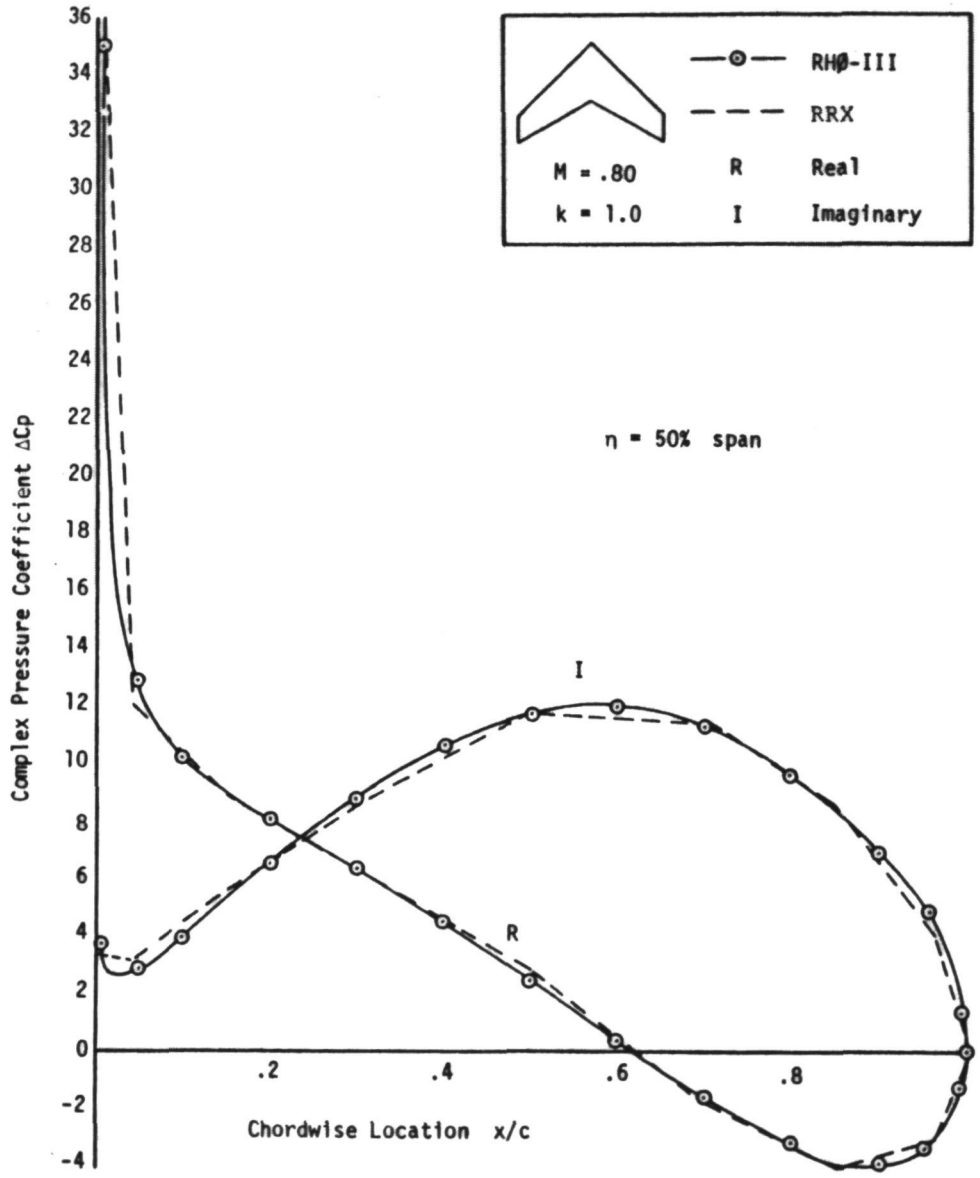

Figure 25.—Comparison of Nonsteady Pressure Using Eight Chordwise Panels—VP1 (C Series)

5.4 VALIDATION PROBLEM TWO

The purpose of VP2 is to run RRX for a surface with a control. The planform, lift coefficient versus reduced frequency, and chordwise pressure distribution are shown in figures 26, 27, and 28. The control surface is a 40% chord full-span flap. The panelization used six equiangular spacings from the leading edge to the hinge line, four equiangular spacings from the hinge line to the trailing edge, and six equiangular spacings across the semispan. The agreement with Rowe is seen to be excellent. Of particular interest is the close agreement in pressure near the leading edge and hinge line, even though no special shape functions were used.

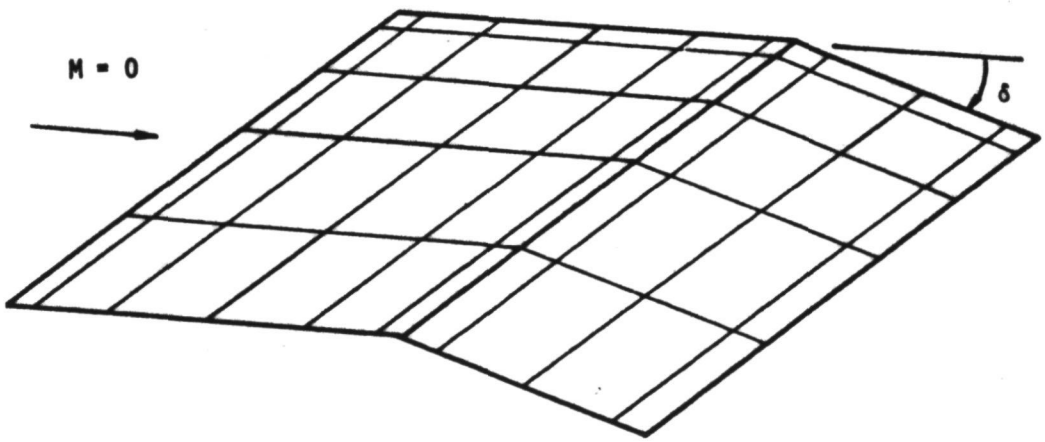

c_f = .4c AR = 2 50 panels k = 0,.5,1.0

Figure 26.—Wing Control Surface—Validation Problem Two

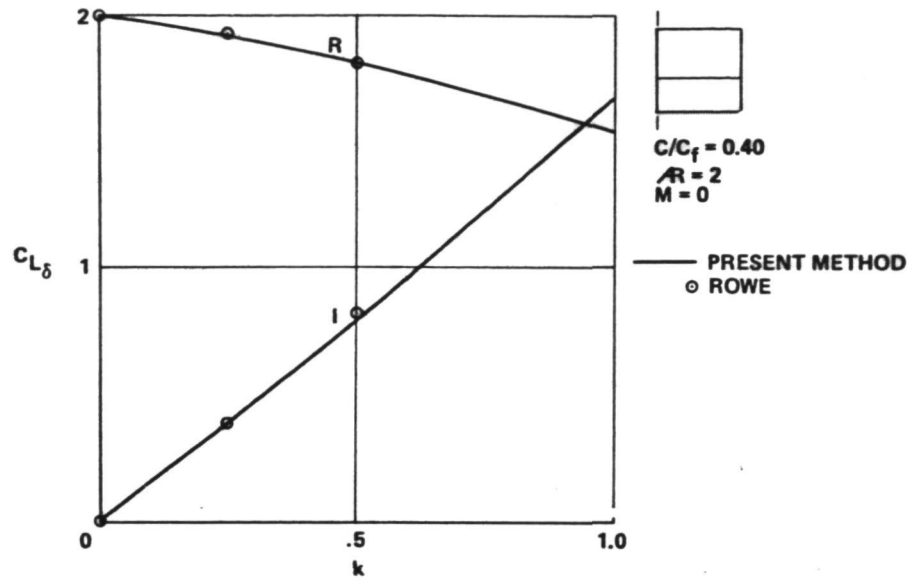

Figure 27.—Lift Coefficient vs Frequency Due to Control Motion—VP2

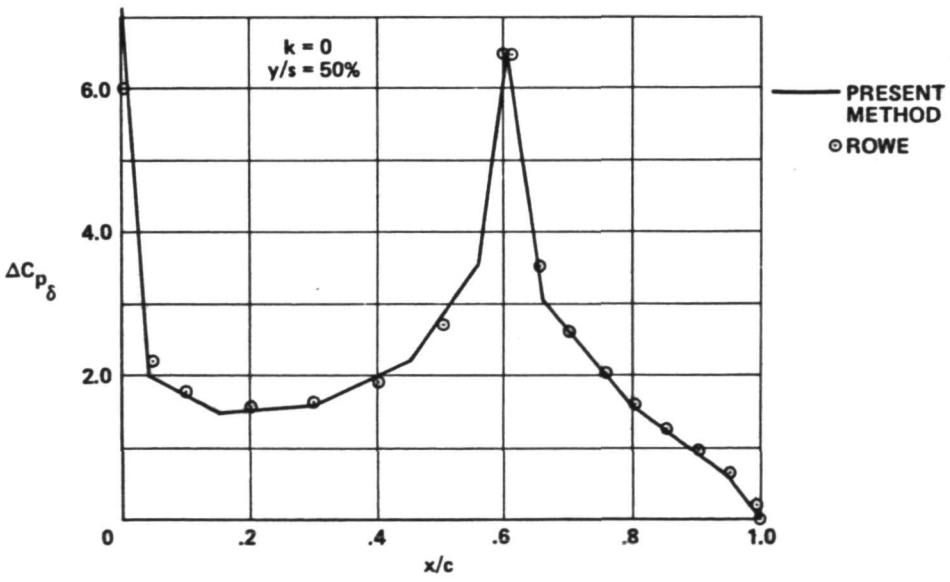

Figure 28.—Chordwise Pressure Distribution Due to Control Motion—VP2

5.5 VALIDATION PROBLEM THREE

The purpose of VP3 is to demonstrate the use of RRX for asymmetrical planforms. Symmetry conditions employed in the present study permit the left planform boundary to be symmetric, antisymmetric, or asymmetric. The results of an asymmetric analysis are shown in figures 29 and 30 for a series of skewed parallelogram planforms with sweep angles ranging from 0^0 to 60^0. The Mach number is 0.80 and the normalwash mode is that of uniform angle of attack. Figure 29 shows the overall center of pressure versus sweep angle, and figure 30 shows the sectional center of pressure.

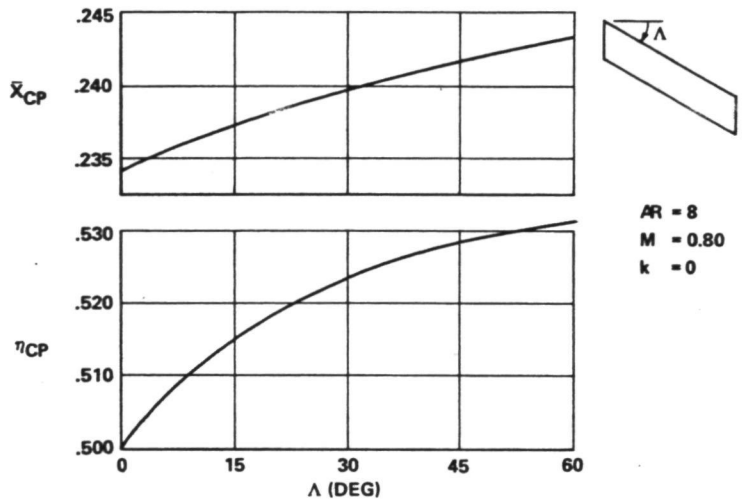

Figure 29.—Overall Center of Pressure for Skewed Wings—VP3

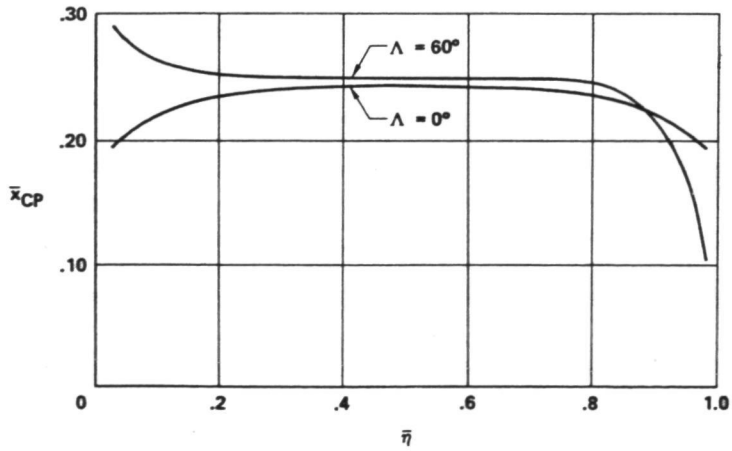

Figure 30.—Sectional Center of Pressure for Skewed Wings—VP3

5.6 VALIDATION PROBLEM FOUR

All results presented so far have been for rigid normalwash distributions. The purpose of VP4 is to demonstrate the use of RRX for flexible modes. The dynamic response to gust loading for a large, subsonic jet transport (including only the wing flexible degrees of freedom) has been calculated* using both the present method and that of Rowe. Figures 31, 32, and 33 compare the results of the present method with those of Rowe for the magnitude of the response amplitudes with fixed controls for wing root shear force, wing root bending moment, and wingtip acceleration, respectively.

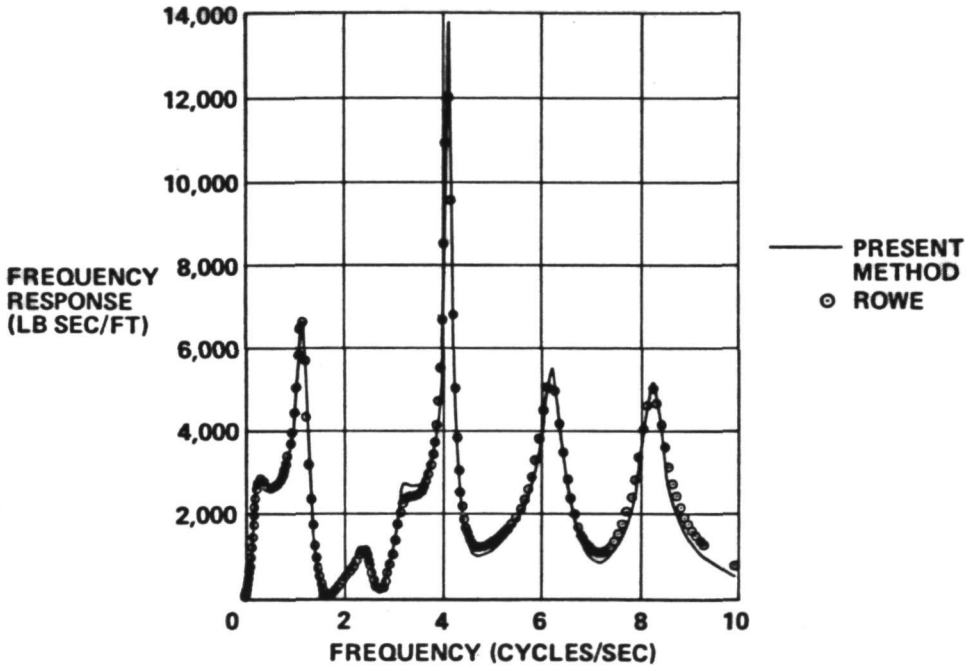

Figure 31.—Wing Root Shear Frequency Response—VP4

*The authors wish to acknowledge the work of R. D. Miller and Richard Kroll in performing these calculations. These calculations were performed under Item 3, Task IV of this study.

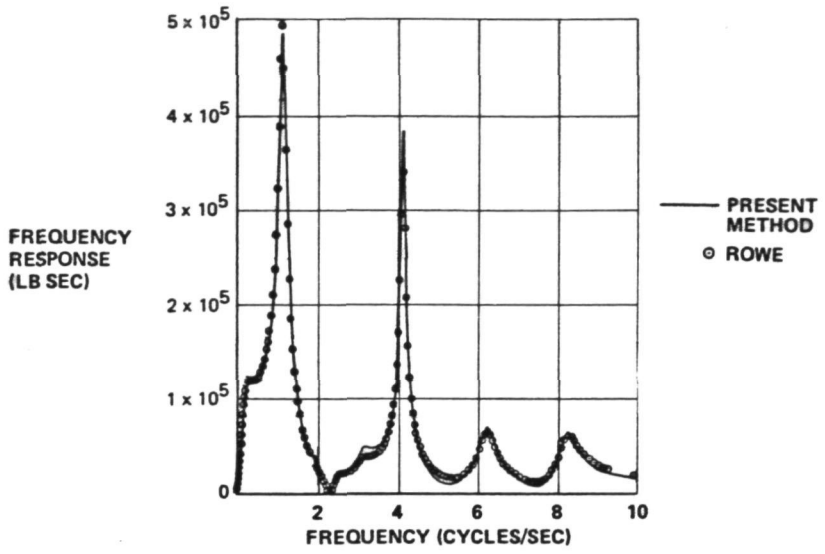

Figure 32.—Wing Root Bending Moment Frequency Response—VP4

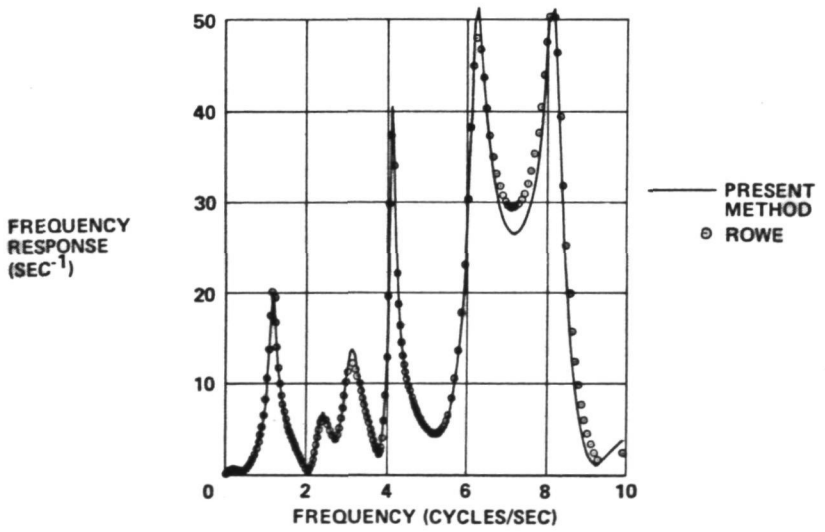

Figure 33.—Wingtip Acceleration Frequency Response—VP4

6.0 CONCLUDING REMARKS

6.1 CURRENT STATUS

The feasibility of using local basis functions for calculating unsteady airloads has been successfully demonstrated. The numerical results show a degree of smoothness and accuracy approaching that of the global basis function methods while retaining the versatility and simplicity of panel methods.

For a given planar aerodynamic surface, Mach number, reduced frequency, and normalwash distribution, the computer code developed during the present study will predict pressure, sectional lift, sectional center of pressure, overall lift, and overall center of pressure. If a control is present, values are calculated for the primary surface and for the secondary (control) surface. In addition, force and moment coefficient matrices can be calculated if desired. Symmetrical, antisymmetrical, and asymmetrical problems can be run.

Potential improvements would be found by extending the method to multiple nonplanar surfaces, incorporating the Landahl-Rowe singularities, implementing a fairing option, providing panel optimization and automation, and optimizing the computational efficiency.

6.2 CONCLUSIONS AND RECOMMENDATIONS

The present study has demonstrated that splined local basis functions formulated in terms of acceleration potential doublets can provide an accurate and useful means for calculating unsteady airloads on flexible aircraft. This work was undertaken as a step toward the eventual goal of defining a method capable of practical application to complete, arbitrarily shaped, three-dimensional configurations, and has served as such.

At the outset it was recognized that local basis functions similar to the ones noted above but formulated in terms of velocity potential doublets, rather than in terms of acceleration potential doublets, might provide a more direct growth capability to general nonplanar, three-dimensional applications. A parallel steady flow research effort by Johnson (ref. 18) utilizing the velocity potential formulation has recently demonstrated a superiority over the earlier steady acceleration potential (or vortex spline) formulation by Mercer (refs. 11 and 12). However, for unsteady flow, the technology for integrating the acceleration potential kernel was readily available, whereas the difficulties associated with integration of the velocity potential doublet were unknown. Hence, a decision was made at the outset to utilize acceleration potential doublets, taking a more conservative approach that would suffice to evaluate the salient behavior of local basis functions in unsteady aerodynamics.

Since that time, the problem of integrating the subsonic velocity potential doublet kernel has been addressed. This unpublished work, carried out by Johnson, suggests integrating, mostly in closed form, the unsteady velocity potential source and doublet kernels with the local basis functions used in the work of reference 18. Thus, it now appears possible to work toward the goal of unsteady analysis of arbitrary three-dimensional configurations by implementing the above mentioned unsteady kernels into the velocity potential approach of reference 18.

Boeing Commercial Airplane Company
P.O. Box 3707
Seattle, Washington 98124
September 15, 1975

APPENDIX A
COMPUTER CODE DESCRIPTION

The sections below describe the RRX code and its use.

A.1 ORGANIZATION

The purpose of the RRX code is to demonstrate the feasibility of using the local basis functions to calculate unsteady airloads, and to do so in a manner that could facilitate its possible application in the future to a FLEXSTAB system. The layout of the code has been determined with these considerations in mind. Figure A-1 depicts five distinct parts of the code, labeled I-V, which approximate the flow within the actual code and separate the work into relatively independent units for purposes of planning.

The bulk of the computing lies in calculating the coefficient matrix, denoted by $[C]$ in part III of figure A-1. From the initial development and numerical analysis viewpoints, part III is the most critical part of the code. Less critical are the input and output interfacers, shown as parts II and V. Solution of the linear algebraic equations is shown in part IV. The solutions may be required in terms of the basis function coefficients or in terms of the inverse of the coefficient matrix, and may be either a determinate collocated solution or an overdetermined complex least squares solution.

A.2 COEFFICIENT MATRIX AND ITS SOLUTION

Denoting by $[C_{mn}]$ the coefficient matrix appearing in equation (4), where m is the downwash index and n is the pressure basis function index, we have

$$\underset{N_W \times 1}{\left\{\frac{w(x_m,y_m)}{V}\right\}} = -\frac{1}{8\pi} \underset{N_W \times N_P}{[C_{mn}]} \underset{N_P \times 1}{\{b_n\}} \qquad \text{(A-1)}$$

Equation A-1 is solved determinately if, and only if, the number N_w of downwash points equals the number N_p of pressure basis functions. The solution may be overdetermined in the sense of complex least square error by using more downwash points than basis functions. In that case, $N_w > N_p$ and (A-1) is replaced by

$$\underset{N_P \times N_W}{[\bar{C}_{mn}]^T} \underset{N_W \times N_W}{[W]} \underset{N_W \times 1}{\left\{\frac{w(x_m,y_m)}{V}\right\}} = -\frac{1}{8\pi} \underset{N_P \times N_W}{[\bar{C}_{mn}]^T} \underset{N_W \times N_W}{[W]} \underset{N_W \times N_P}{[C_{mn}]} \underset{N_P \times 1}{\{b_n\}}, \qquad \text{(A-2)}$$

where $[\bar{C}_{mn}]^T$ denotes complex matrix conjugate transposition and $[W]$ denotes a diagonal matrix of arbitrary positive weighting factors (ref. 20).

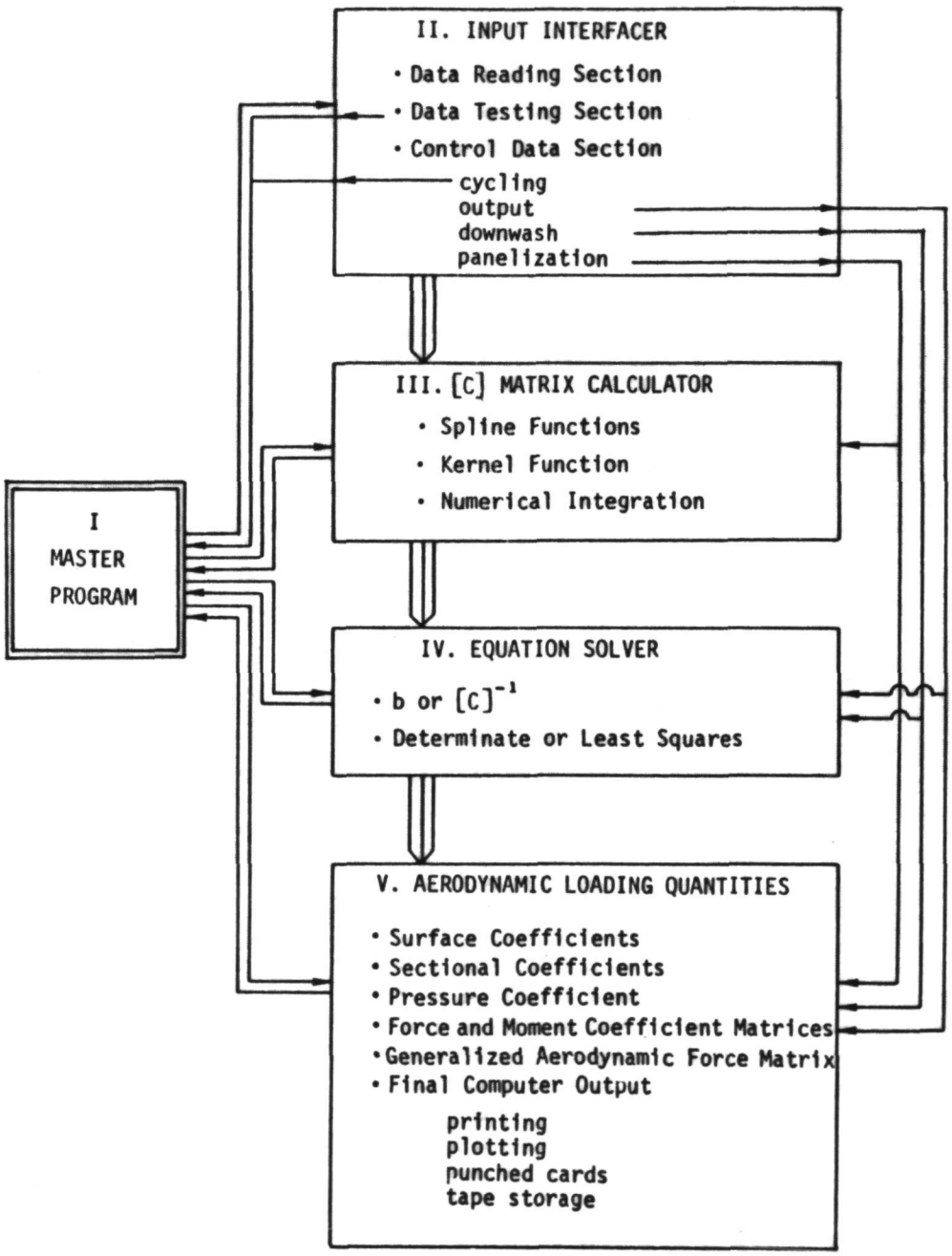

Figure A-1.—Program Organization—Preliminary Layout (Schedule Development Phase)

The actual calculation of the coefficient matrix is performed as described in section 4.2. However, when the left planform boundary intersects a vertical reflection plane (i.e., symmetric or antisymmetric, but not asymmetric), the integration for C_{mn} is extended from the support R_n of P_n to its reflection R_n^* about the left boundary and the value of P_n or R_n^* is equal to, or equal to the negative of, the value of P_n on R_n, depending upon whether the reflection is symmetric or antisymmetric. Thus, for nonasymmetric conditions,

$$C_{mn} = \iint_{\vec{\xi} \epsilon R_n \cup R_n^*} X_n(\vec{\xi})\, P_n(\vec{\xi})\, K_p(\vec{x}_m - \vec{\xi})\, dA, \qquad \text{(A-3)}$$

where X_R is a symmetry-characteristic function,

$$X_n(\vec{\xi}) = \begin{cases} +1 & \vec{\xi} \epsilon R_n \\ +1 & \vec{\xi} \epsilon R_n^* \quad \text{symmetric} \\ -1 & \vec{\xi} \epsilon R_n^* \quad \text{antisymmetric} \end{cases} \qquad \text{(A-4)}$$

Equations (A-3) and (A-4) reduce the number of unknowns by a factor of two when they apply. The dependence of C_{mn} on both downwash location (x_m, y_m) and the location of the support R_n of the basis function P_n is depicted in figure A-2.

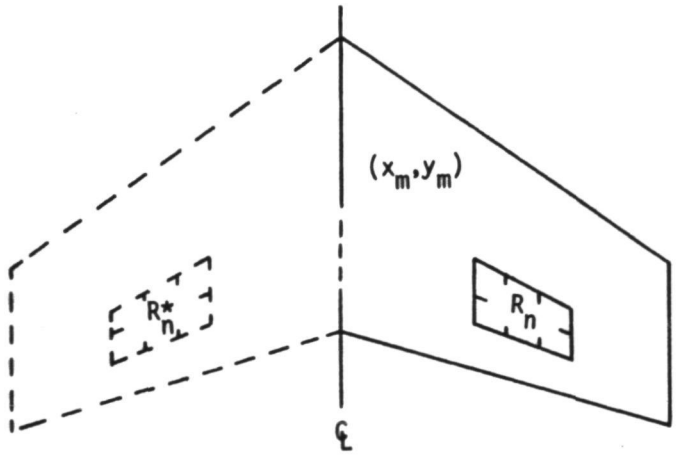

(Reflective Left Boundary Depicted)

Figure A-2.—Downwash Point and Pressure Support for Typical Planform

A.3 PANEL-TO-BASIS-FUNCTION TRANSFORMATIONS

In order to avoid expensive and unnecessary repetitions in calculating the kernel function, the numerical integration must be performed panel by panel. Since the coefficient matrix is defined by the pressure basis function number, it is necessary to determine which pressure basis function supports intersect the panel at hand. This section sets down the necessary equations.

The panels are arranged into N_c rows and N_s columns and are all distinct from one another. The supports, however, overlap in an essential fashion but are arranged also into N_c rows and N_s columns. The number of supports equals the number of panels, and in both cases we number them from 1 to $N_p = N_c N_s$ starting in the first row, proceeding left to right, thence to the second row and so on. This numbering system causes the index to be given in terms of the row and column numbers by equation (5) for both the panels and the basis functions.

Thus, associated with each basis function index n is a set $\bar{N}(n)$ of indices of panels that constitute the support of that basis function. From equation (5),

$$N(n) = \{(\mu-1)\, N_s + \nu : (\mu,\nu) \in \Lambda_n\} \qquad \text{(A-5)}$$

The desired set $N(\bar{n})$ of basis function indices corresponding to a prescribed panel index $\bar{n}$ is therefore the solution to a table lookup problem.

$$(\forall \bar{n}) \quad (N \quad N(\bar{n}) = \{n : \bar{n} \in \bar{N}(n)\} \qquad \text{(A-6)}$$

Equations (4), (A-5), and (A-6) have been programmed into RRX to provide the desired economy in the computation of the kernel function. Further, in the actual code they have been generalized to include general rectangular covers of the basis function supports, rather than the 2 x 3 scheme used in the present study.

A.4 PANELING CONSIDERATIONS

A generic panelization of an aerodynamic surface with a control is depicted in figure A-3. Greater panel density may be needed in regions of rapid changes in pressure. Thus, along the leading-edge, tip, and trailing-edge regions, relatively narrow panels are suggested. In the case shown, where the left planform boundary is a reflective boundary, greater density is not needed there. However, if a control is present, then increased panel densities are required on both sides of the control leading edge and side edges. With only a few additional intermediate panel boundaries, the number of panels can become significant. For the crude example shown, 99 panels are used.

Once the planform boundary and panelization have been specified, the type of splined pressure functions to be employed are determined in accordance with the edge system indicated in figure A-4.

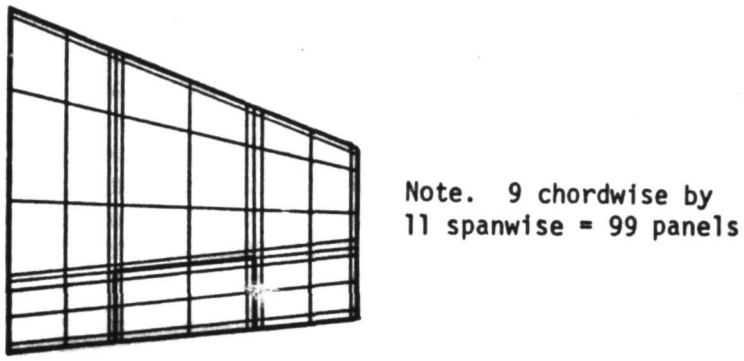

Figure A-3.—Possible Panelization for Primary Surface With Control

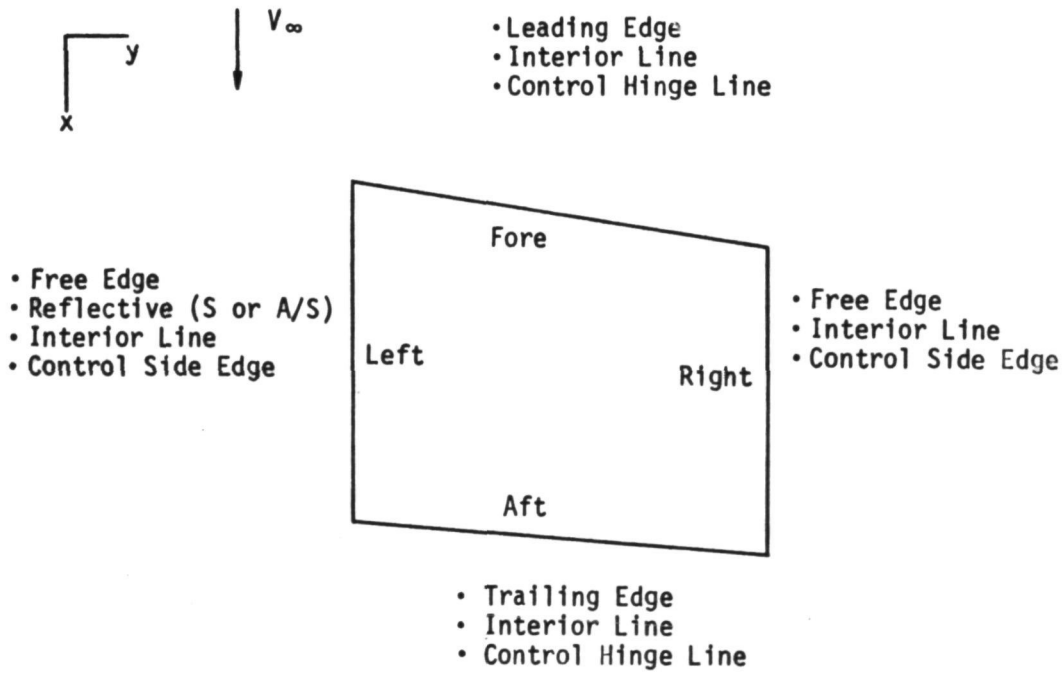

Figure A-4.—Generalized Panel Edge System Used in RRX

A.5 PLANFORM SPECIFICATION

The planform is specified as the union of a number of subsurfaces as depicted in figure A-5. Each subsurface is a trapezoidal area defined by a number of chords as depicted by figure A-6. Each chord is defined by the coordinates of its most upstream point and its length. Specification of the intermediate chord and span stations as shown then suffices to determine the panel boundaries.

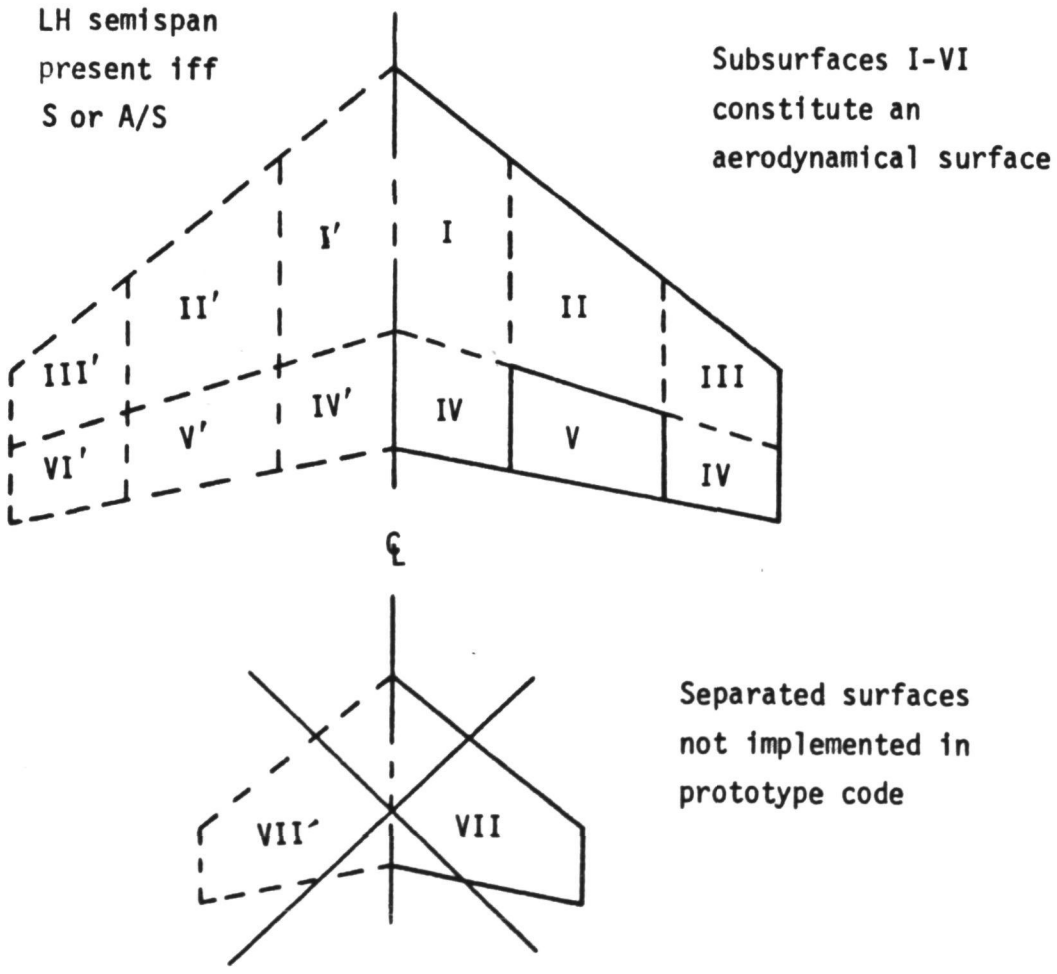

Figure A-5.—Aerodynamical Surface as a Union of Subsurfaces

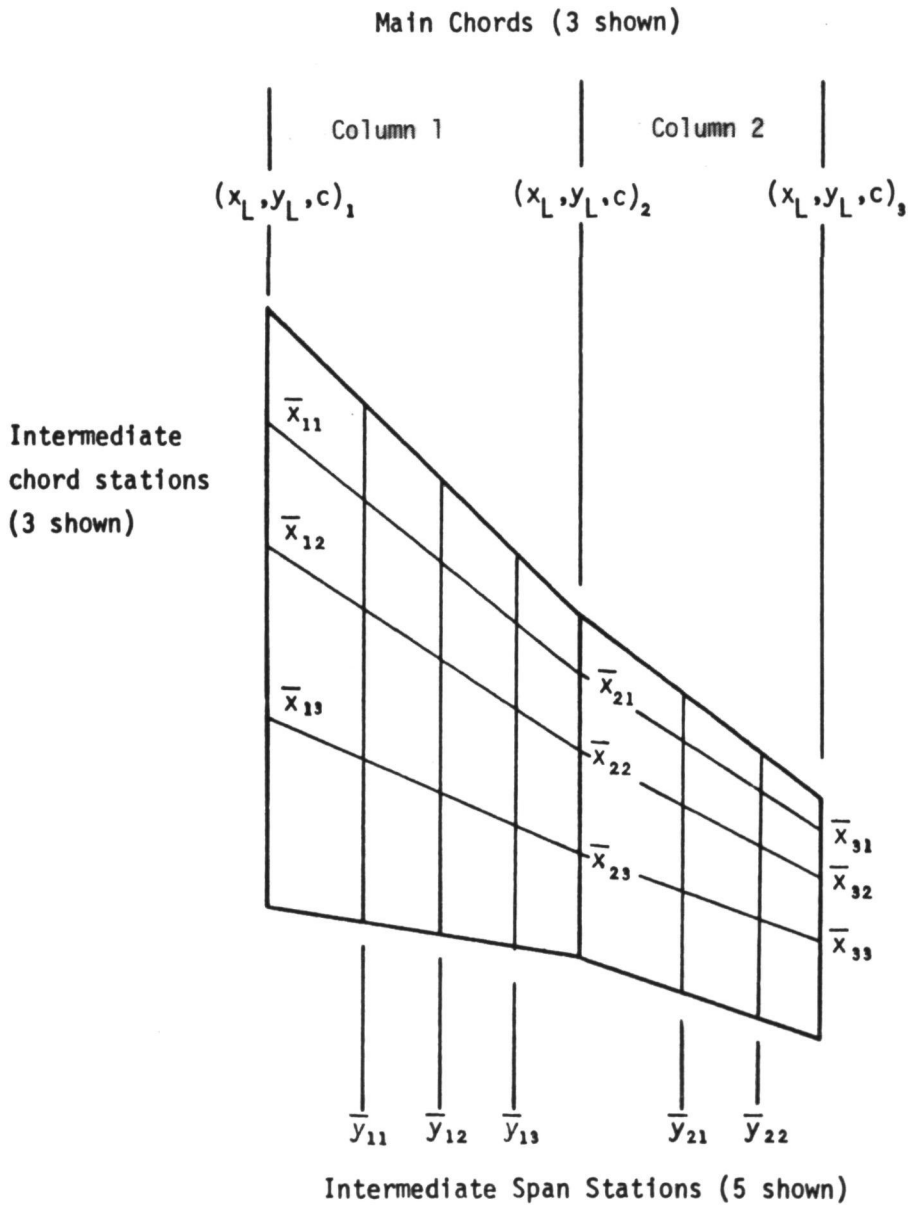

Figure A-6.—Possible Subsurface Scheme for Prototype Code

If a discontinuity exists in the spanwise slope of the planform boundary, as depicted in figure A-7, an inadmissible singularity in downwash results. It is inadmissible in the following sense: the limit of the Küssner operator for smooth edges as the radius of curvature approaches zero does not equal the Küssner operator of the limit function (it is a discontinuous functional). Since the physical flow is smoothed across the boundary layer by the phenomenon of viscosity, it is clear that planform breaks could be faired. One such fairing scheme is depicted in figure A-7 in which the fairing width is some fraction, δ_F, of the width of the boundary trapezoids.

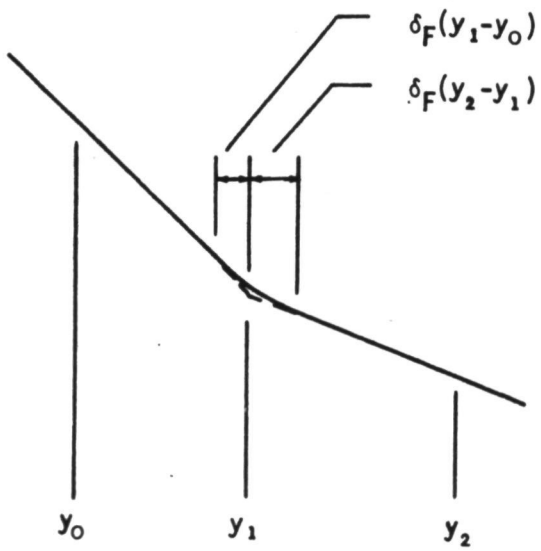

Figure A-7.—Fairing Scheme at Planform Breaks

A.6 AERODYNAMIC LOADING QUANTITIES

Consider the planform configuration depicted in figure A-8.

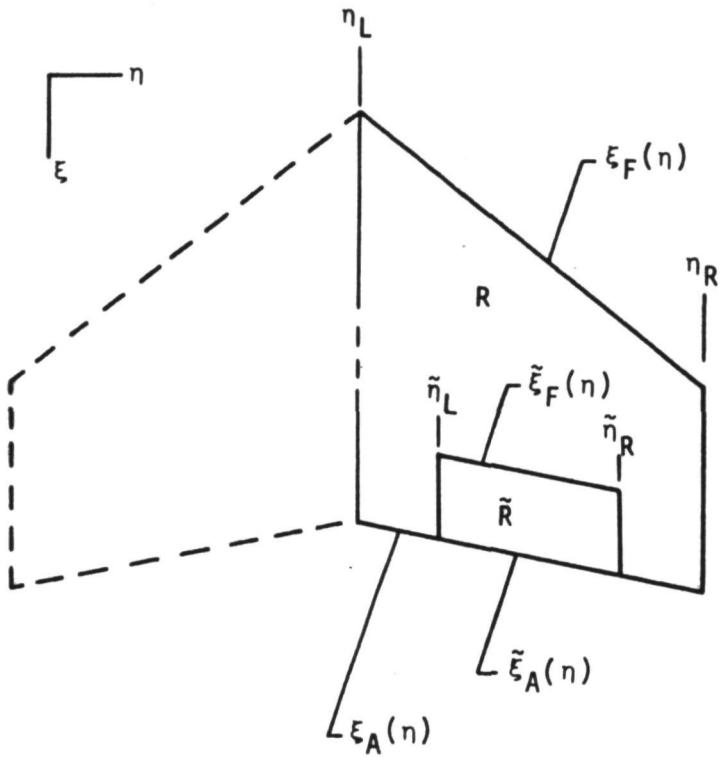

Figure A-8.—Primary and Secondary Surface Nomenclature

Then, using the nomenclature introduced in figure A-8, the following quantities are calculated by the RRX code.

A.6.1 PRESSURE COEFFICIENT

$$\Delta Cp(\xi,\eta) = \sum_{1}^{NP} b_n \, p_n \, (\xi,\eta) \qquad \text{(A-7)}$$

A.6.2 SECTION LIFT COEFFICIENT

$$c_{\ell}(\eta) = \frac{1}{\xi_F(\eta) - \xi_A(\eta)} \int_{\xi_F(\eta)}^{\xi_A(\eta)} \Delta C_p(\xi,\eta)\, d\xi \qquad \text{(A-8)}$$

$$c_{\ell_H}(\eta) = \frac{1}{\tilde{\xi}_F(\eta) - \tilde{\xi}_A(\eta)} \int_{\tilde{\xi}_F(\eta)}^{\tilde{\xi}_A(\eta)} \Delta C_p(\xi,\eta)\, d\xi \qquad \text{(A-9)}$$

A.6.3 SECTIONAL CENTER OF PRESSURE

$$\bar{X}_{cp}(\eta) = \frac{1}{c_{\ell_H}(\eta)} \int_{\xi_F(\eta)}^{\xi_A(\eta)} \frac{\xi - \xi_F(\eta)}{\xi_A(\eta) - \xi_F(\eta)}\, \Delta C_p(\xi,\eta)\, d\xi \qquad \text{(A-10)}$$

$$\bar{X}_{cP_H}(\eta) = \frac{1}{c_{\ell_H}(\eta)} \int_{\tilde{\xi}_F(\eta)}^{\tilde{\xi}_A(\eta)} \frac{\xi - \tilde{\xi}_F(\eta)}{\tilde{\xi}_A(\eta) - \tilde{\xi}_F(\eta)}\, \Delta C_p(\xi,\eta)\, d\xi \qquad \text{(A-11)}$$

A.6.4 SURFACE LIFT COEFFICIENT

$$C_L = \frac{1}{A} \iint_R \Delta C_p(\xi,\eta)\, dA \; ; \; A = \iint_R dA \qquad \text{(A-12)}$$

$$C_{L_H} = \frac{1}{\tilde{A}} \iint_{\tilde{R}} \Delta C_p(\xi,\eta)\, dA \; ; \; \tilde{A} = \iint_{\tilde{R}} dA \tag{A-13}$$

A.6.5 STREAMWISE CENTER OF PRESSURE

$$\xi_{cP} = \frac{1}{C_{L_H} A} \iint_{R} \xi \Delta C_p(\xi,\eta)\, dA \tag{A-14}$$

$$\tilde{\xi}_{cP} = \frac{1}{C_{L_H} \tilde{A}} \iint_{\tilde{R}} \xi \Delta C_p(\xi,\eta)\, dA \tag{A-15}$$

A.6.6 SPANWISE CENTER OF PRESSURE

$$\eta_{cP} = \frac{1}{C_L A} \iint_{R} \eta \Delta C_p(\xi,\eta)\, dA \tag{A-16}$$

$$\tilde{\eta}_{cP} = \frac{1}{C_{L_H} \tilde{A}} \iint_{\tilde{R}} \eta \Delta C_p(\xi,\eta)\, dA \tag{A-17}$$

A.6.7 FORCE AND MOMENT COEFFICIENT MATRICES

1. Definition for loading panel P_ℓ

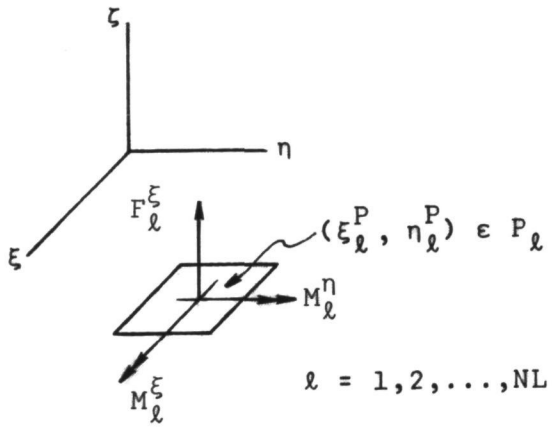

$$\{b_n\} = -8\pi \, [C_{mn}]^{-1} \left\{\frac{w}{v}\right\} \tag{A-18}$$

$$\Delta C_p(\xi,\eta) = -8\pi \lfloor P_n(\xi,\eta) \rfloor \, [C_{mn}]^{-1} \left\{\frac{w}{v}\right\} \tag{A-19}$$

$$F_\ell^\zeta = \iint_{P_\ell} \Delta C_p(\xi,\eta) \, dA \tag{A-20}$$

$$M_\ell^\xi = \iint_{P_\ell} (\eta - \eta_\ell^P) \, \Delta C_p(\xi,\eta) \, dA \tag{A-21}$$

$$M_\ell^\eta = \iint_{P_\ell} (\xi_\ell^P - \xi) \, \Delta C_p(\xi,\eta) \, dA \tag{A-22}$$

Note: F_ℓ^ζ, M_ℓ^ξ and M_ℓ^η have dynamic pressure, $\frac{1}{2}\rho V^2$, factored out.

2. Programmed equations—the coefficient matrices of F_ℓ^ξ, M_ℓ^ξ, and M_ℓ^η with respect to downwash:

$$\underset{NP\times NW}{\left[AIC_{\ell m}^{\xi}\right]} = -8\pi \underset{NL\times NP}{\left[\iint_{P_\ell} P_n(\xi,\eta)\, dA\right]} \underset{NP\times NW}{\left[C_{mn}\right]^{-1}} \qquad (A\text{-}23)$$

$$\underset{NP\times NW}{\left[AIC_{\ell m}^{\xi}\right]} = -8\pi \underset{NL\times NP}{\left[\iint_{P_\ell} (\eta-\eta_\ell^P)\, P_n(\xi,\eta)\, dA\right]} \underset{NP\times NW}{\left[C_{mn}\right]^{-1}} \qquad (A\text{-}24)$$

$$\underset{NP\times NW}{\left[AIC_{\ell m}^{\eta}\right]} = -8\pi \underset{NL\times NP}{\left[\iint_{P_\ell} (\xi_\ell^P-\xi)\, P_n(\xi,\eta)\, dA\right]} \underset{NP\times NW}{\left[C_{mn}\right]^{-1}} \qquad (A\text{-}25)$$

Note: If the least squares solution is used ($N_w > N_p$), the generalized inverse from (A-2) must be substituted for the indicated inverse.

A.6.8 GENERALIZED AERODYNAMICAL FORCES

The generalized aerodynamical force coefficient matrix defined earlier has not been programmed into the RRX code. For future reference, however, the equation to program this important quantity is displayed below. It should be noted that the essential practical difficulty lies in the proper interpolation of the structural modes since, in practice, their continuum distributions are seldom known.

$$A_{rs} = -8\pi \iint_R \phi_r^{(z)}(\xi,\eta)\, \lfloor P_n(\xi,\eta)\rfloor\, dA\, [C_{mn}]^{-1} \left\{\frac{w}{V}\right\}_{\text{mode s}} \qquad (A\text{-}26)$$

"Page missing from available version"

REFERENCES

1. Ashley, H.; and Rodden, W. P.: "Wing-Body Aerodynamic Interaction," *Annual Review of Fluid Mechanics,* vol. 4, pp 431-472, 1972.

2. Landahl, M. T.; and Stark, V. J. E.: "Numerical Lifting Surface Theory—Problems and Progress." *AIAA Journal,* vol. 6, no. 11, pp 2049-2060, 1968.

3. Ashley, H.; Widnall, S.; and Landahl, M. T.: "New Directions in Lifting Surface Theory." *AIAA Journal,* vol. 3, no. 1, pp 3-16, 1965.

4. Morino, L.; and Kuo, C. C.: *Unsteady Subsonic Compressible Flow Around Finite Thickness Wings.* AIAA paper 73-213, 1973.

5. Küssner, H. G.: "Allgemeine Tragflachentheorie." *Luftfahrtforschung,* vol. 17, no. 11/12, pp 310-378, 1940 (translation NACA TM 979).

6. Watkins, C. E.; Runyan, H. L.; and Woolston, D. S.: *On the Kernel Function of the Integral Equation Relating the Lift and Downwash Distributions of Oscillating Finite Wings in Subsonic Flow.* NACA report 1234, 1955.

7. Watkins, C. E.; Woolston, D. S.; and Cunningham, H. J.: *A Systematic Kernel Function Procedure for Determining Aerodynamic Forces on Oscillating or Steady Finite Wings at Subsonic Speeds.* NASA TR-R 48, 1959.

8. Hsu, P. T.: *Calculation of Pressure Distributions for Oscillating Wings of Arbitrary Planform in Subsonic Flow by the Kernel Function Method.* MIT-ASRL TR 64-1, 1957.

9. Rowe, W. S.; Winther, B. H.; and Redman, M. C.: "Unsteady Subsonic Loadings Caused by Control Surface Motions." *Journal of Aircraft,* vol. 11, no. 1, pp 45-54, 1974.

10. Rowe, W. S.; Sebastian, J. D.; and Redman, M. C.: "Some Recent Developments in Predicting Unsteady Loadings Caused by Control Surface Motions." To be published in *AIAA Journal,* late 1975.

11. Mercer, J. E.; Weber, J. A.; and Lesford, E. P.: *Aerodynamic Influence Coefficient Method Using Singularity Splines.* NASA CR 2423, 1974.

12. Mercer, J. E.; Weber, J. A.; and Lesford, P. E.: *Aerodynamic Influence Coefficient Method Using Singularity Splines.* AIAA paper 73-123, 1973.

13. Prandtl, L.: "Allgemeine Betrachtungen über die Strömung zusammendrückbarer Flüssigkeiten." *ZAMM,* vol. 16, no. 3, pp 129-142, 1936.

14. Hadamard, J.: *Lectures on Cauchy's Problem in Linear Partial Differential Equations.* Yale University Press, 1923.

15. Watson, G. N.: *Theory of Bessel Functions.* Cambridge University Press, 2nd edition, 1958.

16. Landahl, M. T.: "Pressure-Loading Functions for Oscillating Wings and Control Surfaces." *AIAA Journal,* vol. 6, no. 2, pp 345-348, 1968.

17. Rowe, W. S.; Winther, B. A.; and Redman, M. C.: *Prediction of Unsteady Aerodynamic Loadings Caused by Trailing Edge Control Surface Motions in Subsonic Compressible Flow–Analysis and Results.* NASA CR-2003, 1973.

18. Johnson, F. T.; and Rubbert, P. E.: *Advanced Panel-Type Influence Coefficient Methods Applied to Subsonic Flows.* AIAA paper 75-50, January 1975.

19. Multhopp, H.: "Methods for Calculating the Lift Distribution of Wings." *British ARC R&M 2884,* 1950.

20. Fromme, J. A.: "Least Squares Approach to Unsteady Kernel Function Aerodynamics." *AIAA Journal,* vol. 2, no. 6, pp 1349-1350, 1964.